JGR Solid Earth

RESEARCH ARTICLE
10.1029/2024JB029763

Stress Heterogeneities Governed by Fault Structure and Stress Transfer: The 2016–2017 Central Italy Seismic Sequence

Patricia Martínez-Garzón[1,2], **Men-Andrin Meier**[3], **Cristiano Collettini**[4], **Federica Lanza**[3], and **Georg Dresen**[1]

[1]GFZ Helmholtz Centre for Geosciences, Potsdam, Germany, [2]RWTH University of Aachen, Aachen, Germany, [3]Swiss Seismological Service, ETH Zurich, Zurich, Switzerland, [4]Sapienza University of Rome, Rome, Italy

Key Points:

- Stress inversions from a deep learning focal mechanism catalog illuminate spatio-temporal stress field heterogeneities at various scales
- Stress heterogeneities at 1–10 km scale are related to fault structures and coseismic stress near the ruptures of the largest earthquakes
- Stress regimes depend on depth suggesting an interplay between shallow normal faults and a detachment horizon at depth

Supporting Information:

Supporting Information may be found in the online version of this article.

Correspondence to:

P. Martínez-Garzón,
patricia@gfz.de

Citation:

Martínez-Garzón, P., Meier, M.-A., Collettini, C., Lanza, F., & Dresen, G. (2025). Stress heterogeneities governed by fault structure and stress transfer: The 2016–2017 central Italy seismic sequence. *Journal of Geophysical Research: Solid Earth*, *130*, e2024JB029763. https://doi.org/10.1029/2024JB029763

Received 20 JUN 2024
Accepted 25 JUL 2025

Author Contributions:

Conceptualization: Patricia Martínez-Garzón, Men-Andrin Meier, Cristiano Collettini
Data curation: Men-Andrin Meier, Federica Lanza
Formal analysis: Patricia Martínez-Garzón, Men-Andrin Meier
Investigation: Patricia Martínez-Garzón, Men-Andrin Meier, Cristiano Collettini, Georg Dresen
Methodology: Patricia Martínez-Garzón
Software: Patricia Martínez-Garzón, Men-Andrin Meier
Supervision: Georg Dresen
Validation: Men-Andrin Meier

Abstract

We analyze the evolution of stress parameters from the 2016–2017 central Italy seismic sequence taking advantage of ∼13,747 robust focal mechanisms from a deep learning catalog. The density of the catalog allows us to invert focal mechanisms over distances of a few km and different time periods. We inferred a number of stress-related parameters, including the fault plane variability, the orientation of principal stress axes and maximum horizontal stress, the relative magnitudes of principal stresses and the variability of the principal stress orientations with respect to the median. From the uniform regional stress field consistent with the extension of the Apennine Belt, we observe local stress heterogeneities that are driven by the structural features and the coseismic stress history. A variation of the principal stress magnitudes and regimes from pure normal faulting toward transtension with depth is observed. Stress differences at the 1–10 km wavelength are observed between each side of two of the main regional fault structures. The reported stress results suggest a partial mechanical coupling and a strong interaction between the shallow normal faults and the detachment horizon at depth. Furthermore, distinct trends are observed in the stress parameters after the largest mainshocks, and before the M_W 6.5 Norcia mainshock, potentially indicating the high shear stress still available in well oriented faults after the M_W 6.0 Amatrice earthquake. Our analysis holds implications toward (a) constraining stress magnitudes, (b) illuminating the interaction between the shallow normal faults and detachment horizons, and (c) tracking stress evolution during seismic sequence.

Plain Language Summary

Deep learning catalogs of focal mechanisms can offer a better understanding of the state of stress. We focused on the 2016–2017 seismic activity in central Italy. By analyzing a catalog containing ∼13,747 high quality focal mechanisms, we are able to study stress parameters such as the orientation of stress axes, stress magnitudes, and variations in the stress field over time and space. The seismic sequence in central Italy unfolded on normal faults, consistent with the regional stress pattern. In space, we illuminated stress variations at different depth ranges, with the depth range between 2.5 and 8.0 km displaying pure normal faulting stress and a mixed normal faulting and strike-slip stress regimes above and below. We also observe stress differences related to main regional fault structures. These differences could have influenced the rupture of large earthquakes on these faults. Our study identified stress changes following major earthquakes, particularly at depths below 4 km. In time, variations in stress ratios at different depths before large earthquakes suggest a partial mechanical connection between them. This analysis provides insights into stress patterns in central Italy, aids in understanding earthquake dynamics on normal faults, and sheds light on the interaction between shallow and deep seismic activity.

1. Introduction

The stress field orientation and its magnitudes are controlled by various forces and mechanisms operating at diverse and mutually superposed spatial and temporal wavelengths. On a regional scale, (e.g., 100–1000 s km), the stress field is controlled primarily by plate tectonic motions, which define plate kinematics and the dynamics of plate deformation (e.g., Heidbach et al., 2010; Lundstern & Zoback, 2020; M. L. Zoback, 1992). However, there is an ever-growing body of observations at regional (∼10–100 km) and local (∼1–10 km) scales revealing that the stress pattern can substantially differ from that predicted by the plate motions (Heidbach et al., 2007; Martínez-Garzón et al., 2020). At intraplate regions far from a plate boundary and in mountain belts, gravity forces and flexure of the crust can dominate the stresses (Dalmayrac & Molnar, 1981; Levandowski et al., 2016,

Visualization: Cristiano Collettini, Federica Lanza
Writing – original draft: Patricia Martínez-Garzón, Cristiano Collettini, Georg Dresen
Writing – review & editing: Patricia Martínez-Garzón, Men-Andrin Meier, Cristiano Collettini, Federica Lanza, Georg Dresen

2018). Seasonal fluctuations related, for example, to water level changes and temperature (Johnson et al., 2017), anthropogenic activities (Martínez-Garzón et al., 2013; Schoenball et al., 2014), or stress transfer from the occurrence of earthquakes (Hardebeck, 2012; Hardebeck & Hauksson, 1997; Martínez-Garzón et al., 2016) may affect or even overprint the stress pattern imposed by plate tectonics. The presence of geological structures such as faults, folds, detachments, salt diapirs and sedimentary basins (Heidbach et al., 2007; Nikolinakou et al., 2014; Yin, 1989) tends to rotate the local stress field orientation because of the mechanical contrast between the units (M. D. Zoback, 2007). Changes in rock density and topography result in variations of the gravitational forces affecting both the orientation of the principal stress axes and their magnitudes (Abolfathian et al., 2020; Fialko, 2006). This range of forces and varying rock and structural properties can result in heterogeneities in the stress pattern, affecting stress magnitudes (i.e., magnitude of the principal stresses), orientation of the principal stress axes and earthquake stress drops.

Quantifying spatial and temporal variations in the orientation and magnitude of the stress field is essential for determining seismic hazard and understanding the dynamics of earthquake sequences, as the local stress field (e.g., in the scale of a few km) plays a strong role in earthquake nucleation, propagation, and arrest. For example, a heterogeneous stress field may result from smaller isolated asperities that eventually rupture and arrest (e.g., foreshocks), while a more homogeneous stress state across different fault segments may allow an earthquake rupture to propagate further and hence result in a larger earthquake (Ben-Zion et al., 2003; Hardebeck, 2014; Zaliapin & Ben-Zion, 2021).

An important topic is whether stress heterogeneities are primarily controlled by mechanical discontinuities of the medium, thus remaining stable with time, or if they evolve over time and space. For example, in a recent review, Li and Cai (2022) described a broad scatter of stress magnitude measurements over short distances, highlighting how local structural and material heterogeneity might influence the principal stress magnitudes even at similar depth. Numerical simulations of earthquakes on heterogeneous faults have shown that mainshocks tend to break stronger asperities, that is, the ones that are able to sustain the largest peak stresses, while weaker asperities tend to rupture within the foreshock sequence (Cattania & Segall, 2021). Observations from more indirect stress proxies such as the Brune earthquake stress drops of well-recorded $M < 4$ events also tend to support that fault properties such as damage, geometry (Ruhl et al., 2023) and tectonic regime (Allmann & Shearer, 2007; Chen et al., 2024) control the distribution of stress drops, while temporal variations are comparably smaller.

Deep learning catalogs now offer a new opportunity to re-examine the processes associated with earthquake crustal dynamics at a much higher resolution. In recent years, the application of artificial intelligence (AI) techniques to earthquake phase picking and association problems (e.g., Zhu & Beroza, 2019; Zhu et al., 2022) has yielded a wealth of high-resolution seismicity catalogs typically containing up to 10 times more events than traditional catalogs (e.g., Becker et al., 2024; Tan et al., 2021). Similarly, novel methodologies to facilitate the generation of dense deep learning earthquake focal mechanism catalogs have been developed (e.g., Ross et al., 2018). The extent to which these deep learning catalogs can help investigations of earthquake physics, and their overall contribution to the earthquake forecasting problem, is only now starting to be explored (e.g., Beroza et al., 2021; Cheng et al., 2023; Cochran et al., 2023; Mancini et al., 2022; Martínez-Garzón et al., 2023). Deep learning focal mechanism catalogs open a new window to resolve stress parameters at much higher resolution. The inversion of earthquake focal mechanisms is the only available methodology to determine stress parameters across the entire seismogenic thickness (e.g., Michael, 1987). As focal mechanisms are a proxy for the planes of co-seismic strain release in the crust, it is commonly assumed that the orientations of the stress and strain fields are similar and that the earthquakes slip on the direction of the applied shear stress (Bott, 1959; Twiss & Unruh, 1998; Wallace, 1951).

In this study, our goal is to address the following scientific questions: (Q1) Using stress tensor inversion of enhanced seismicity and focal mechanism catalogs, do we observe stress heterogeneity at wavelengths of a few km and what are the main factors affecting it? (Q2) Is the stress field across the seismogenic layer influenced by the presence of deeply-rooted detachment horizons? and (Q3) Does stress analysis from the inversion of seismic data provide indication of the stress evolution of a fault system toward upcoming larger events? To this end, we image spatio-temporal variations in stress parameters during the 2016–2017 central Italy seismic sequence. In this sequence, three mainshocks, namely the M_w 6.0 Amatrice, M_w 5.9 Visso and M_w 6.5 Norcia, nucleated on normal faults with kinematics consistent with the regional stress field.

2. Seismo-Tectonics of the 2016–2017 Central Italy Seismic Sequence

Previous analyses of the stress field across the Italian peninsula have employed the data available from the World Stress Map (WSM) project (Heidbach et al., 2010) combining stress indicators from borehole breakouts, focal mechanisms, and selected stress inversions (e.g., Montone et al., 2004, 2012; Pierdominici & Heidbach, 2012). At a tectonic scale, the Italian peninsula displays overall N-S compression due to the convergence of the African and Eurasian plates. The Apennines fold-and-thrust belt formed in the late Miocene to early Pliocene. Since the late Pliocene, however, the region has been subjected to NE-SW to ENE-WSW extension with current rates of 2.5–3.5 mm/yr (Carafa et al., 2020; Lavecchia et al., 1994; Stemberk et al., 2019). Extension is accommodated by a network of active normal faults striking mainly NNW-SSE. Extension is partitioned between seismogenic faulting and potential reactivation of detachment horizons (Boncio et al., 2000; Collettini et al., 2022; Michele et al., 2020), with possible viscous flow at depth >10 km as suggested by modeling of geodetic data (Carafa et al., 2020; Mandler et al., 2021). Formal stress inversions from WSM focal mechanisms for the Mediterranean region revealed heterogeneities in the S_{HMax} orientation at a scale of tens of kms, particularly for tectonically complex regions such as the Alps and the Calabrian arc (Martínez-Garzón et al., 2020). The 2016–2017 central Italy seismic sequence occurred in an active normal fault system cutting through the former fold and thrust belt of the Apennines. The region is separated into different geological and structural domains by the Monte Sibillini Thrust (MST) controlling seismicity distribution and faulting styles (Barchi et al., 2021, Figure 1).

The 2016–2017 Central Italy seismic sequence is characterized by three $M_{\mathrm{W}} \geq 5.9$ mainshocks, namely the 24 August M_{W} 6.0 Amatrice, 26 October M_{W} 5.9 Visso and 30 October M_{W} 6.5 Norcia. The deployment of a seismic network as soon as the first $M_{\mathrm{W}} > 5$ earthquake of this sequence allowed high-resolution recording of the seismicity (Chiaraluce et al., 2017; Michele et al., 2020). The catalog was further enhanced using AI techniques for phase picking and earthquake association (Tan et al., 2021). This catalog showed that the seismicity did not only localize along the main fault structures, but also indicated the presence of active areas with more distributed deformation. The Amatrice and Norcia mainshocks nucleated at a depth of about 6 km and the Visso mainshock at a shallower depth <5 km. All mainshocks occurred along SW-dipping normal faults (Brozzetti et al., 2019; Pizzi et al., 2017; Pucci et al., 2017). The seismic sequence continued evolving, particularly south of the MST, where three earthquakes with M_{W} 5.3 and one with M_{W} 5.4 (referred to as the Campotosto earthquake) occurred on 18 January 2017 activating dip-slip faults (Chiaraluce et al., 2017).

Geological cross-sections constructed by merging surface geology, seismic reflection profiles and borehole data suggested that the mainshocks occurred near the intersection of the southwest-dipping normal faults with different regional thrusts formed during the earlier compressional phase (Barchi et al., 2021). At depth >6 km, that is, below the mainshock hypocenters, the seismicity is distributed within sub-horizontal imbricated bands. Sub-horizontal earthquake distribution and extensional focal mechanisms have been used to propose the presence of a basal detachment fault (Chiaraluce et al., 2017; Vuan et al., 2017) that in some places is fragmented (Waldhauser et al., 2021). The partial correspondence of these patches of distributed seismicity with Triassic Evaporites lithology has also been attributed to the ductile and brittle rheology of evaporites layers above or along the inferred basal detachment (Collettini et al., 2022).

A normal faulting stress regime with predominant NE-SW extension has been reported for the area covered by the 2016–2017 central Italy sequence (Chiaraluce et al., 2017; Mariucci & Montone, 2016). However, the present-day seismic and mechanical interaction between the local normal faults, cross-cutting thrusts and detachment horizons in the deeper part, suggest that the stress field might display subtle variations at local (1 g. 1–10 km) scale (e.g., Kemna et al., 2021). The primary goal of this study is to evaluate whether we can resolve such stress variations and elaborate on the main mechanisms driving the local stress during a seismic sequence.

3. Data and Methods

3.1. Seismic Catalog and Focal Mechanisms

The starting point for our analysis is the deep learning focal mechanism catalog derived in Meier (2025) and Meier et al. (2025). In this work, the authors utilized an earthquake catalog derived with machine learning containing about 900,000 seismic events recorded during the time period from the 2016 M_{W} 6.0 Amatrice earthquake on 24 August 2016, 01:36:32 UTC up to 17 August 2017, 00:00:00 UTC (Tan et al., 2021). The reported median relative hypocenter location uncertainties of this catalog are 36, 56, and 87 m, for the two horizontal and the vertical directions, respectively. The event magnitudes range from M_W −0.5 to 6, and the magnitude of completeness was estimated to be M_C 0.3 (Tan et al., 2021).

Based on this catalog, Meier (2025) and Meier et al. (2025) used a convolutional neural network classifier modified after Ross et al. (2018) to pick the first motion polarity of the ∼15 million P-phase arrivals detected by Tan et al. (2021). Meier (2025) and Meier et al. (2025) then used the SKHASH algorithm (Skoumal et al., 2024) to compute ∼40,523 focal mechanisms over the same time span as the Tan et al. (2021) hypocenter catalog. We focused our study on the highest quality subset with a fault plane uncertainty ≤20°, yielding a total of 13,747 best-constrained focal mechanisms (Figure 1a). This amounts to ∼1.5% of all events in the hypocenter catalog, and covers the magnitude range between M_W 0 and 4.6. Accordingly, the largest earthquakes of the sequence were not included. The fault plane uncertainty of this subset of focal mechanisms does not show any remarkable trends with depth and time (Figure S1 in Supporting Information S1). We selected four temporal intervals as follows (Figure 1a):

T1: From the origin time of the Amatrice mainshock (24 August 2016, 01:36:32 UTC) up to just before the origin time of the Norcia mainshock (30 October, 06:40:17 UTC), and including also the third largest earthquake (Visso, 26 October, 19:18:05 UTC). This period yielded 2,950 focal mechanisms from the subset with fault plane uncertainty ≤20°.
T2: From the origin time of the Norcia mainshock to 5 December 2016 representing a time period of early Norcia aftershocks and seismicity, yielding 4,024 focal mechanisms from the subset with fault plane uncertainty ≤20°.
T3: From 5 December 2016 up to just before the Campotosto earthquake (18 January 2017, 10:16:40 UTC), representing a time period without strong immediate aftershock sequences and comprising a total of 2,780 focal mechanisms from the subset with fault plane uncertainty ≤20°.
T4: From the origin time of the Campotosto earthquake (18 January 2017, 10:16:40 UTC) to the end of the catalog (14 August 2017, 06:45:02 UTC). This last time period comprised 3,993 focal mechanisms from the subset with fault plane uncertainty ≤20°.

3.2. Discretization of Focal Mechanisms and Stress Tensor Inversion

The choice of how the seismicity is grouped can influence the results of the subsequent stress inversions (e.g., Hardebeck, 2006; Townend & Zoback, 2004). For this reason, it is important to discretize the data set as objectively as possible. Here, we started with a procedure as described in Martínez-Garzón et al. (2016). Adopting a Cartesian coordinate system, we discretized the focal mechanisms from each time period T1–T4 into 3D spatial clusters. We first split the seismicity according to *k*-means clustering, which is a way of grouping earthquakes together into clusters. The method starts with a pre-defined number of random seeds distributed over the area of the earthquakes, and progressively converges into the final clusters to minimize the nearest neighbor distance. We chose the number of clusters that yielded the largest silhouette coefficient, which is a measure of how similar an object is to its own cluster compared to other clusters (Rousseeuw, 1987). Preserving this first split, we subsequently grouped the focal mechanisms into optimal clusters using *k*-means and imposing a minimum number of 45 focal mechanisms per cluster. This choice is based on previous synthetic analyses testing the minimum number of focal mechanisms needed for obtaining accurate stress orientation results considering focal mechanism uncertainty (Martínez-Garzón et al., 2016).

The clusters defined for each time range were inverted for the stress field using the MSATSI linear stress tensor inversion (Martínez-Garzón et al., 2014), which is an adaptation from the original linear stress inversion developed in Michael (1984, 1987) and further adapted to create a smoother stress field by considering the stress field orientation from adjacent regions, if desired (Hardebeck & Michael, 2006). The main purpose of employing a damped inversion is to remove variations that are not strongly required by the data. As here we applied an iterative event clustering methodology to select the optimal volumes to invert for stress field, which has the effect of smoothing variations, we set the damping parameter to zero.

As in Martínez-Garzón et al. (2016), we combined this stress inversion with the iterative stress inversion approach presented in Vavryčuk (2014). In each iteration, the two fault planes from each focal mechanism are compared to the stress field orientation from the previous iteration, and the fault plane best oriented for failure within that stress field is selected according to the Mohr-Coulomb criterion (Vavryčuk, 2014). The 95% confidence interval of the stress parameters obtained by the inversion is estimated by bootstrap resampling of the original focal mechanism

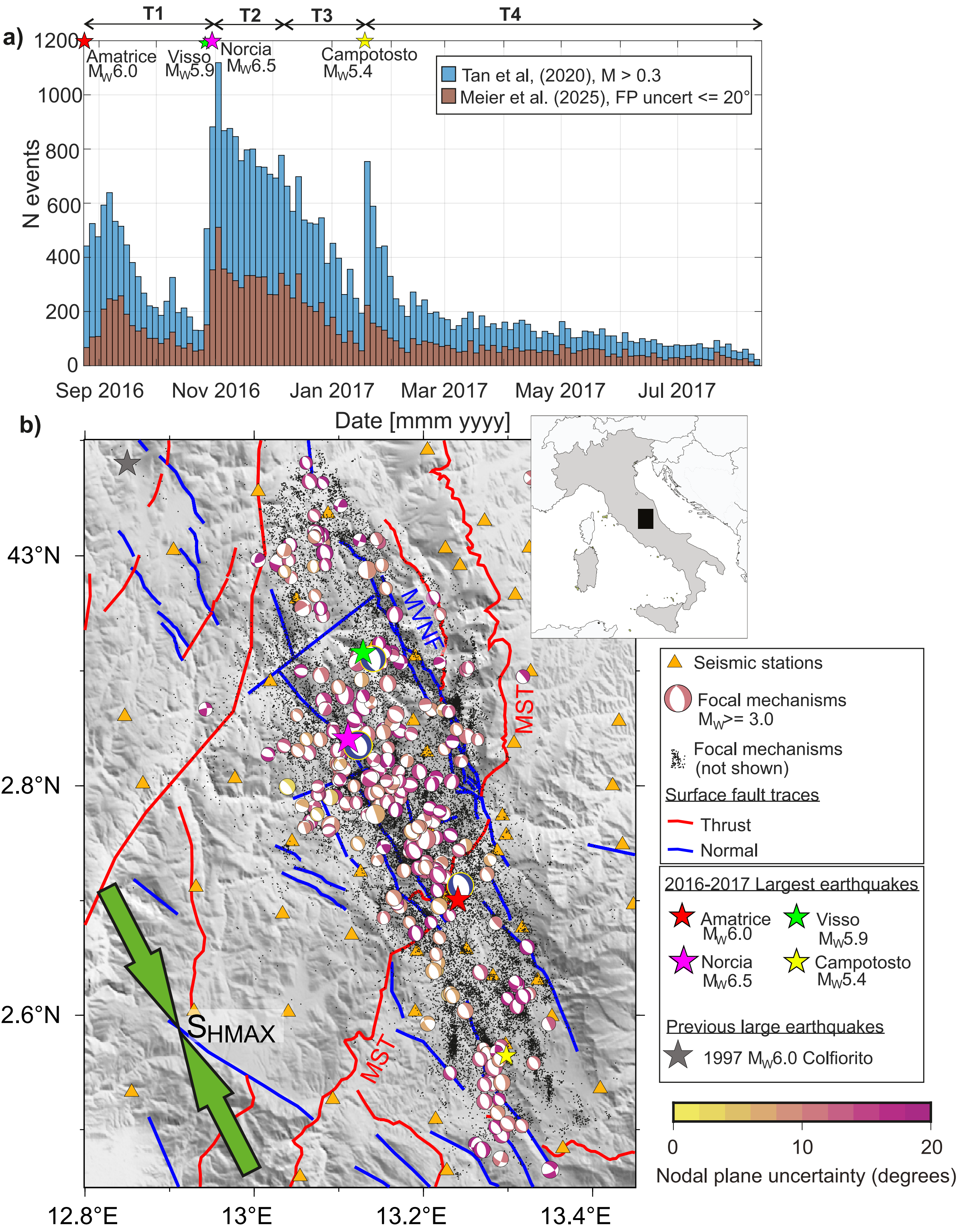
T1
T2
T3
T4
a)
Amatrice MW6.0
Visso MW5.9
Norcia MW6.5
Campotosto MW5.4
Tan et al, (2020), M > 0.3
Meier et al. (2025), FP uncert <= 20°
N events
0
200
400
600
800
1000
1200
Sep 2016
Nov 2016
Jan 2017
Mar 2017
May 2017
Jul 2017
Date [mmm yyyy]
b)
43°N
42.8°N
42.6°N
12.8°E
13°E
13.2°E
13.4°E
MVNF
MST
MST
SHMAX
Seismic stations
Focal mechanisms MW>= 3.0
Focal mechanisms (not shown)
Surface fault traces
Thrust
Normal
2016-2017 Largest earthquakes
Amatrice MW6.0
Visso MW5.9
Norcia MW6.5
Campotosto MW5.4
Previous large earthquakes
1997 MW6.0 Colfiorito
0
10
20
Nodal plane uncertainty (degrees)

Figure 1.

data set (2,000 samples randomly selected with replacement) and repeating the stress tensor inversion (see e.g. Hardebeck & Michael, 2006; Michael, 1987).

As every run of the *k*-means algorithm starts with spatially distributed, random seeds, the algorithm yields different clusters in each run. Hence, for each time interval, we performed 20 iterations of the clustering algorithm and subsequent stress inversion results. Then, we combined the focal mechanisms and stress inversion results from the different iterations event-wise, by calculating the median of the corresponding parameter per event over all the runs in which each particular event was used. We focused on analyzing the following parameters:

(i) The median focal mechanism variability $\widehat{\varphi_f}$ within each cluster, quantifying the heterogeneity included in a group of focal mechanisms. $\widehat{\varphi_f}$ is calculated as the median from the distribution of Kagan angles (Kagan, 1991) between each pair of focal mechanisms forming the cluster (Kwiatek et al., 2024; Martínez-Garzón et al., 2016).
(ii) Orientation of the maximum horizontal stress S_{HMax}, which is calculated following Lund and Townend (2007).
(iii) The stress ratio R as defined by ($R = \frac{S_1 - S_2}{S_1 - S_3}$).

In each crustal volume, we classified the stress regime according to the trend and plunge angles of the three principal stress axes as normal faulting, strike-slip, reverse and oblique faulting, following M. L. Zoback (1992).

(iv) For crustal volumes displaying a stress regime as defined above, we calculated the Anderson fault parameter A_{PHI} (Simpson, 1997 see also Lundstern, 2024): $A_{PHI} = (n + 0.5) + (-1)^n \cdot (0.5 - R)$, where $n = 0$, 1, and 2 represents normal, strike-slip and reverse fault types, respectively. According to this definition, $A_{\mathrm{PHI}} = 0$ (radial normal faulting) represents a case where $S_{\mathrm{V}} >> S_{\mathrm{HMax}} = \mathrm{S}_{\mathrm{hmin}}$, $A_{\mathrm{PHI}} = 0.5$ represents a pure normal faulting regime, and $A_{\mathrm{PHI}} = 1$ a transtensional faulting regime (mixed strike-slip and normal faulting regime).
(iv) Deviation from the regional orientation of the principal stress axes φ_σ. We defined the regional orientation of the stress tensor with the trend and plunge of the S_1 and S_3 axes given as S_1 [196, 78], S_3 [151, 8] (Montone et al., 2012). We then quantified the difference between the regional stress orientation and the orientation of the principal stress axes for any cluster using the Kagan angle (Kagan, 1991) applied to a tensor.

4. Results

4.1. Focal Mechanism Variability Related to the Presence of Fault Structures

We find that the median variability of the focal mechanisms $\widehat{\varphi_f}$ varies across fault structures. The most prominent trend observed is a difference in $\widehat{\varphi_f}$ between events located on either side of the surface trace of the MST, which is a prominent regional fault structure that also marks the boundary of the Umbria-Marche, Laga and Gran Sasso geological domains (Barchi et al., 2021; Collettini et al., 2022). For the time periods T1 (between the Amatrice and the Norcia mainshocks) and T4 (after the M_{W} 5.4 Campotosto earthquake), $\widehat{\varphi_f}$ is larger on the NW side of the surface projection of the MST (Figures 2a and 2c; Figure S2 in Supporting Information S1). In contrast, the focal mechanisms are more homogeneous SE of the surface projection of the MST (Figures 2a and 2c, Figure S2 in Supporting Information S1).

Likewise, we also find different $\widehat{\varphi_f}$ patterns in the hanging wall and footwall on either side of the fault segments activated by the Norcia and Amatrice mainshocks (Scognamiglio et al., 2018; Tinti et al., 2016). Again, for the periods T1 (Figure 2b) and T4 (Figure S3 in Supporting Information S1), $\widehat{\varphi_f}$ is larger in the footwall than in the hanging wall of the activated fault. Extending the rupture plane of the Norcia mainshock toward depth >6.5 km into the sub-horizontal seismically active zone, $\widehat{\varphi_f}$ remains larger in the footwall region of the normal fault. These

Figure 1. The 2016–2017 central Italy seismic sequence. (a) Histogram of seismicity rates from the Tan et al. (2021) seismicity catalog (blue bars) and focal mechanisms with fault plane uncertainty ≤20° utilized in this study (Meier, 2025; Meier et al., 2025, orange bars). Upper horizontal arrows mark the temporal periods T1–T4 into which we divided the data set. (b) Seismotectonic setting of the seismic sequence. Black dots represent the seismic events for which a focal mechanism with fault plane uncertainty ≤20° is available (orange bars in a). Plotted beach balls show the focal mechanisms (Meier, 2025; Meier et al., 2025) with fault plane uncertainty ≤20° and $M_{\mathrm{W}} \geq 3.0$. Solid thick lines show the surface traces from normal (blue) and thrust (red) fault structures (Barchi et al., 2021). MST: Monte Sibillini Thrust. MVNF: Monte Vettore Normal Fault. Green inward arrows highlight the regional S_{HMax} orientation derived from focal mechanisms and borehole breakouts (Chiaraluce et al., 2017; Montone et al., 2004, see text for details).

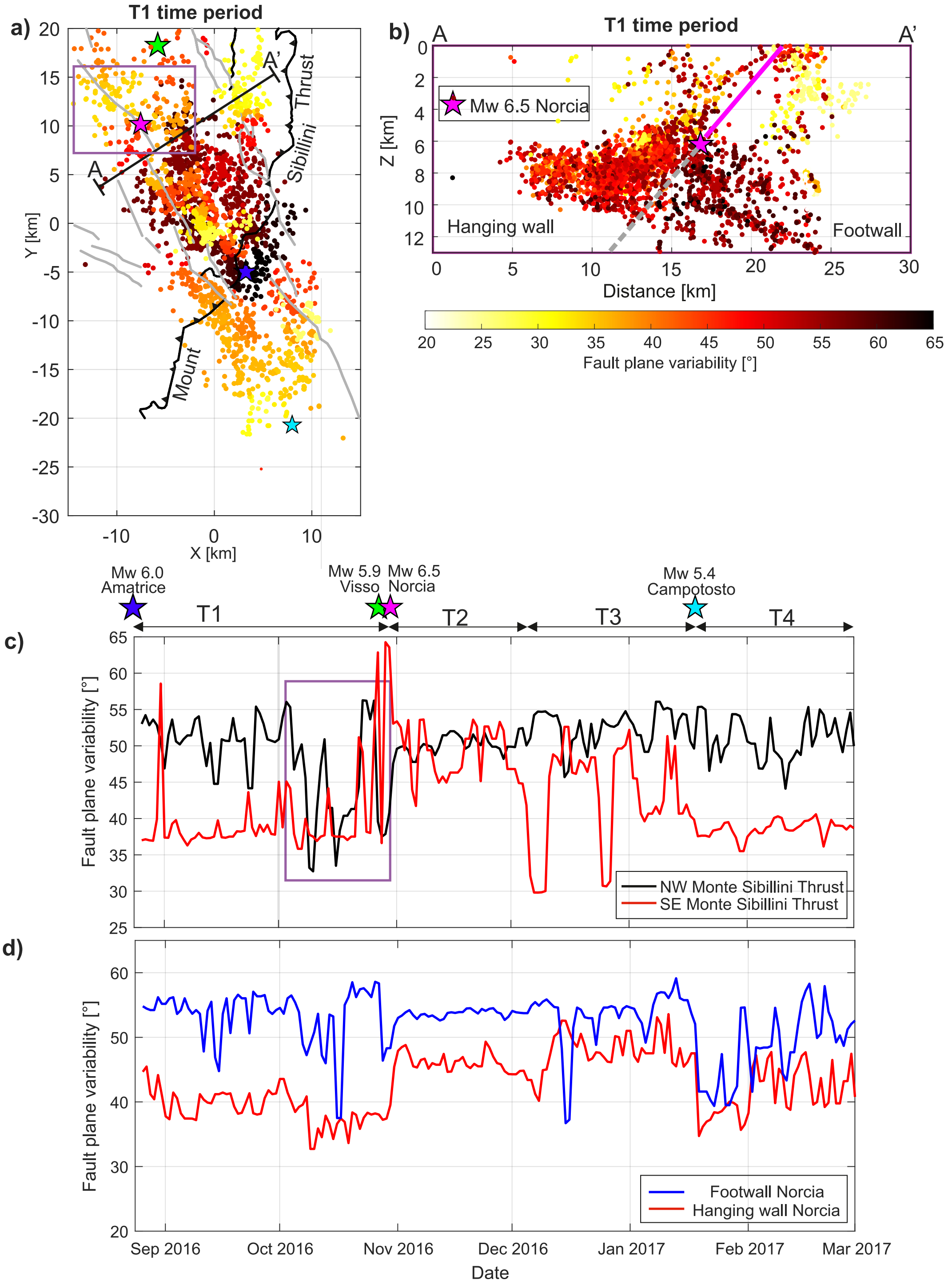

Figure 2. Spatio-temporal distribution of the median fault plane variability $\widehat{\varphi_f}$. (a) Spatial distribution (map view) of the $\widehat{\varphi_f}$ for the time period T1. Black and gray lines indicate surface expression of major fault structures. (b) Profile depth section (along A-A′ line) distribution of $\widehat{\varphi_f}$ at each side of the M_W 6.5 Norcia earthquake rupture plane for time period T1. (c) Temporal evolution of $\widehat{\varphi_f}$, with black and red lines representing the values from the northwestern and southeastern sides of the Monte Sibillini Thrust (MST), respectively. Points are calculated every 2 days. (d) Same as (a) but separating the seismicity from the footwall (blue) and hanging wall (red) of the fault that ruptured the M_W 6.5 Norcia mainshock (purple continuous line in (b)) and extending it below 6.5 km (dashed gray line in (b)). In (c), the four time periods T1–T4 inverted separately are marked in the upper panel. Dark blue, green, magenta and cyan stars mark the origin time of the M_W 6.0 Amatrice, M_W 5.9 Visso, M_W 6.5 Norcia and M_W 5.4 Campotosto earthquakes, respectively. In panels (a) and (b) purple rectangle marks the period and area displaying lower fault plane variability around the Norcia epicenter discussed in the text.

differences are less prominent for the T2 and T3 temporal periods (Figures S2 and S3 in Supporting Information S1).

In addition to spatial variations, we also resolved the evolution of $\widehat{\varphi_f}$ in time. To do this, we assigned to each individual focal mechanism the fault plane variability of the spatial cluster in which it was included. Then we sorted the events temporally and calculated the median value of the fault plane variability considering windows of 2 days and moving every day. The stress evolution during the T1 time period is of particular interest to understand the patterns after the M_W 6.0 Amatrice and before the M_W 6.5 Norcia earthquakes. About 1 month before the M_W 6.5 Norcia earthquake, a decrease of $\widehat{\varphi_f}$ of about 10° is observed on the NW side of the surface projection of the MST (purple rectangle in Figure 2c). Notably, the future Norcia epicenter falls within a region displaying lower fault plane variability (purple rectangle in Figure 2c). Starting December 2016, the temporal evolution of $\widehat{\varphi_f}$ contains stronger variabilities over short times (Figures 2c and 2d). These larger variabilities could be related to the decay of the sequence, which possibly results in a more spatially heterogeneous distribution of seismicity from different parts of the analyzed area.

4.2. Overview of Stress Inversion Results and Relation to Regional Stress Field

From our high-resolution stress analysis, we retrieve a predominantly normal faulting stress regime with a median S_{HMax} orientation trending ∼N154°E and a median A_{PHI} of ∼0.4 during the entire analyzed time (Figure 3a). Both, stress regime and the average S_{HMax} orientation are consistent with the current NE-SW extension of the Apennines and with previous studies based on stress indicators from the WSM (Montone et al., 2004) and focal mechanisms of the largest aftershocks of this sequence (Chiaraluce et al., 2017).

Beyond the homogenous stress pattern of the entire analyzed region, the resolved S_{HMax} orientations and A_{PHI} parameters show local (1–10 km) spatial and temporal stress variations for the different clusters (Figure 3, Figure S3 in Supporting Information S1). In space, the largest stress variations are related to the presence of fault structures, as it will be shown in Section 4.3 (Figures 4 and 5). In time, stresses vary with respect to the occurrence of the largest earthquakes of the seismic series. Relative stress magnitudes also vary substantially with depth and temporal periods. We classified our obtained stress tensor orientations into normal, strike-slip, reverse, and oblique stress regimes (Anderson, 1951) as proposed in M. L. Zoback (1992). The depth interval between 2.5 and 8.0 km depth displays a striking dominance of normal faulting regime over all analyzed time periods (Figure 3c, Table S1 in Supporting Information S1). At depths shallower than 2.5 km, there are clusters displaying oblique regime, contributing up to 17% and 8% of all clusters/bins for the time periods T1 and T2, respectively. Likewise, there are clusters displaying oblique and strike-slip stress regimes at depth >8.0 km, with up to 19% and 10% of the inversions (Table S1 in Supporting Information S1), and most prominent during the T1 and T2 time periods.

4.3. Spatial and Depth Variations in Stress Parameters

The most prominent lateral variation in the stress pattern at the wavelengths of tens of kms is observed approximately at either side of the M_W 6.1 hypocenter. On the NW side, the S_{HMax} orientation is predominantly trending around 165° (Figure 4a). In contrast, to the SE, the S_{HMax} orientation is rotated anticlockwise up to 30° (Figure 4a). The different stress states are also reflected in the A_{PHI} parameter (Figure 5a, Figure S4 in Supporting Information S1). Smaller A_{PHI} values near 0.25 are observed for some areas in the NW toward a radial normal faulting regime with $S_V > S_{\mathrm{HMax}}$, while on the SE, we observe areas with A_{PHI} values reaching almost 0.75, hence representing a transtensional stress regime (Figure 3a, Figure S4 in Supporting Information S1). Just east of the Amatrice epicenter, we find a local stress heterogeneity displaying a strike-slip stress regime for all analyzed time periods (Figure S4 in Supporting Information S1).

Distinct variations of the A_{PHI} parameter and some small variations in the S_{HMax} orientations are observed with depth, with a general trend that appears relatively consistent in time. From the surface to about 2.5 km depth, some clusters of seismicity display A_{PHI} values reaching almost one (i.e., Figure 5a, section AA', T1), hence representing mixed normal-strike-slip. The seismicity from this depth range is occurring in a geological layer of mixed carbonates (Barchi et al., 2021; Collettini et al., 2022) and was observed to be activated mainly during T1, that is, between the occurrence of the Amatrice and the Norcia mainshocks (Figures 3 and 5, Table S1 in Supporting Information S1). The observed strike-slip stress regime activating shallow seismicity is probably due to the vertical stress being reduced at shallow depth, as the magnitude of the vertical stress S_v is proportional to the

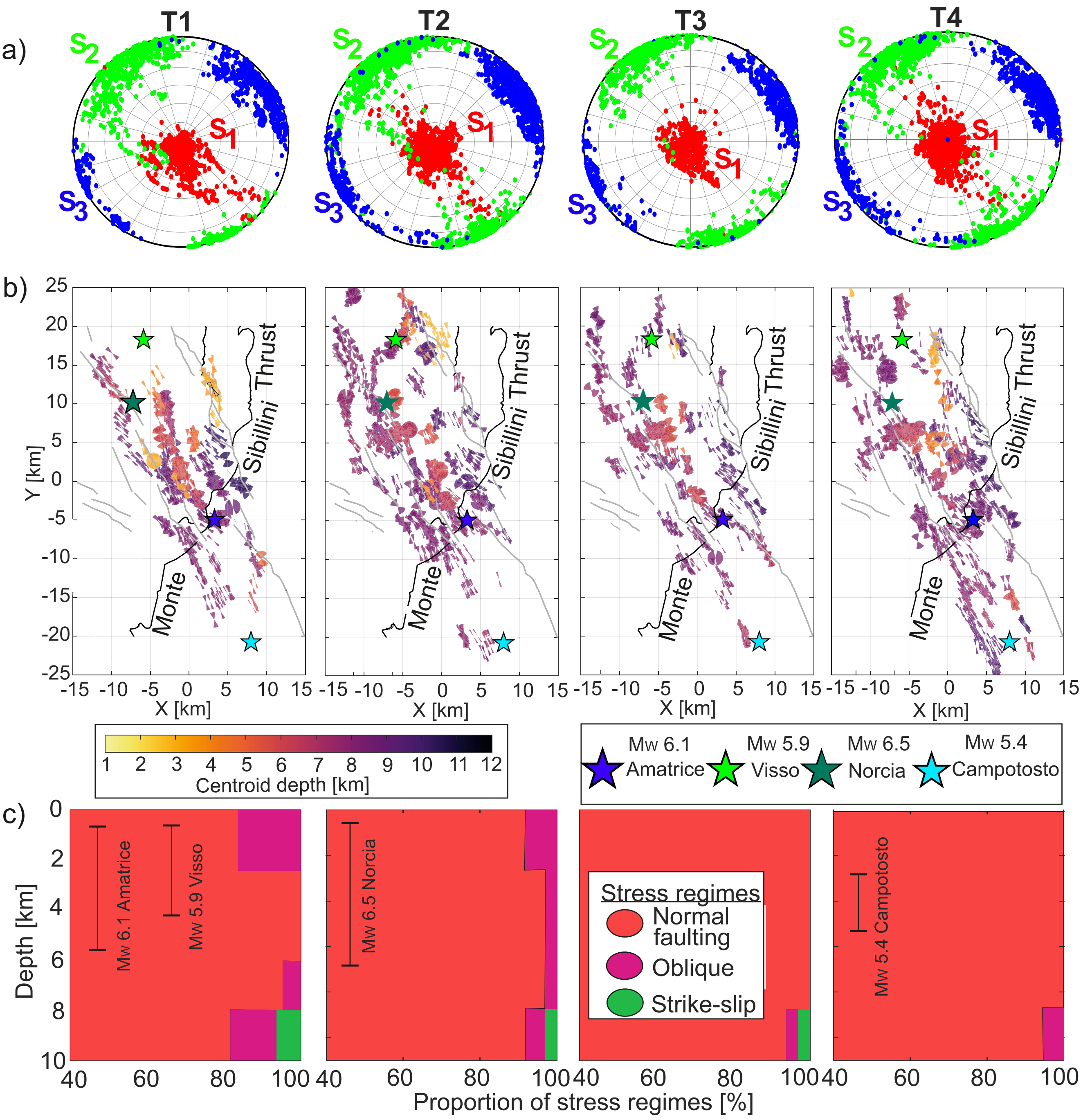

Figure 3. Summary of stress tensor inversion results for each temporal period. (a) Upper panel: Stereonets showing the principal stress orientations from all stress inversions in the considered time period. (b) Spatial distribution of S_{HMax} orientation for time intervals T1–T4 analyzed separately. Each fan symbol represents a stress tensor inversion result, with the width of the fan representing the 95% confidence interval of the S_{HMax} estimates. Each fan is color encoded with the depth of the corresponding cluster centroid. (c) Area plots showing the proportion of each stress regime with depth estimated for the four analyzed time intervals. For reference, the depth range of the largest earthquakes included in each time period is plotted as a vertical bar.

weight of the lithospheric column. In addition, at shallow crustal depth partial reactivation of strike-slip structures inherited from the compressional tectonic phase may occur (e.g., Collettini et al., 2005). The depth range between 2.5 and 6.5 km is located within the stratigraphic unit of the carbonates and Triassic evaporites (Barchi et al., 2021; Collettini et al., 2022) and holds an almost constant A_{PHI} pattern with time (Figure 5b, Table S1 in Supporting Information S1), with a strikingly dominant normal faulting stress regime characterized by a low A_{PHI}

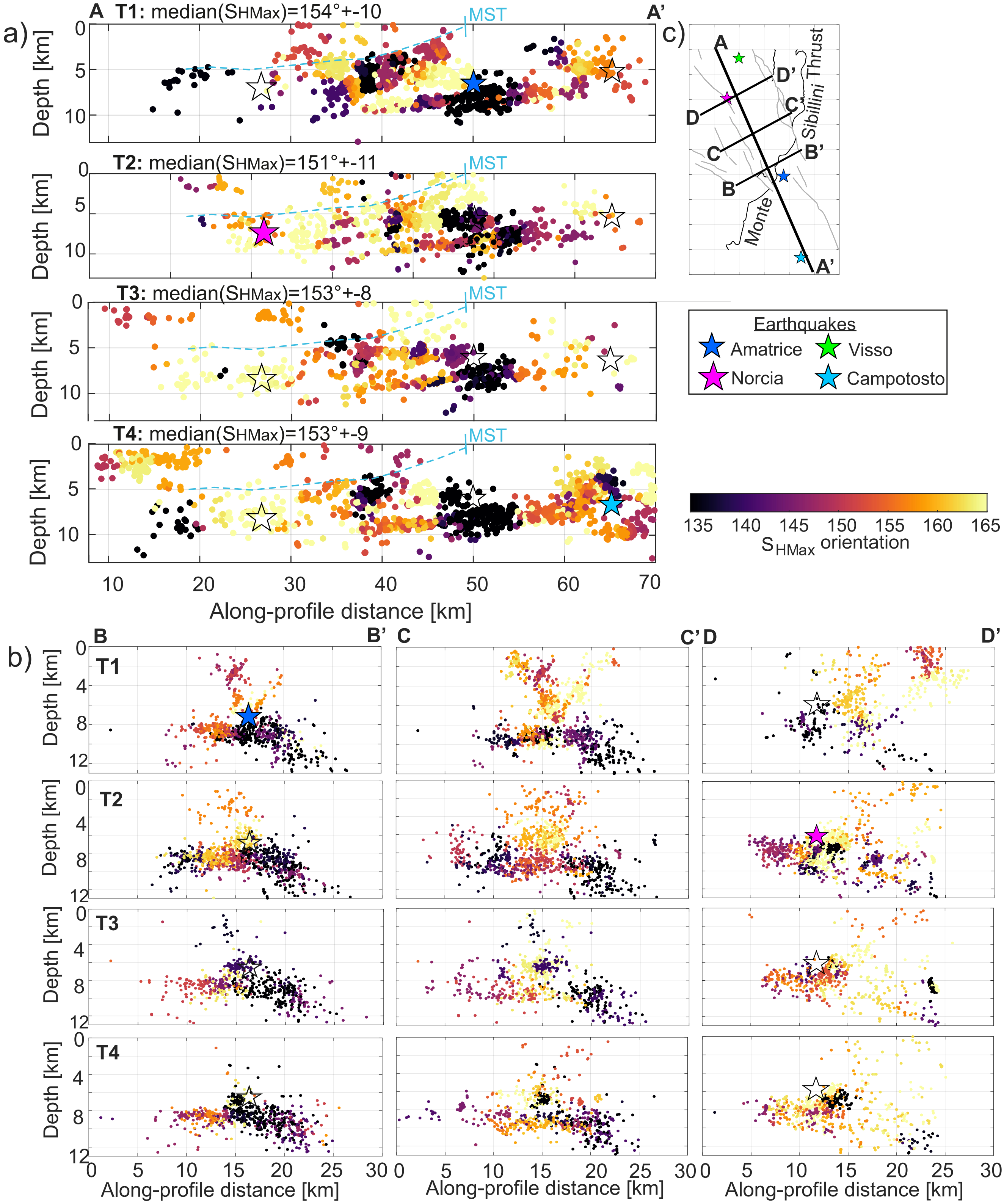
a)
A
T1: median(SHMax)=154°+-10
A'
MST
T2: median(SHMax)=151°+-11
T3: median(SHMax)=153°+-8
T4: median(SHMax)=153°+-9
Depth [km]
0
5
10
10
20
30
40
50
60
70
Along-profile distance [km]
c)
A
D'
D
C'
C
B'
B
A'
Sibillini Thrust
Monte
Earthquakes
Amatrice
Visso
Norcia
Campotosto
135
140
145
150
155
160
165
SHMax orientation
b)
B
B'
C
C'
D
D'
T1
T2
T3
T4
0
4
8
12
0
5
10
15
20
25
30
Along-profile distance [km]

Figure 4.

~0.25 ($S_V > S_{HMax} \sim S_{hmin}$). This is particularly evident in the area south of the Norcia epicenter (Figure 5b, cross section DD'). In this region, similar magnitudes of S_{HMax} and S_{hmin} may lead to complex fault patterns (De Paola et al., 2009). The inferred A_{PHI} suggests $S_{HMax} \sim S_{hmin}$, in agreement with the observed larger uncertainties in the S_{HMax} and S_{hmin} orientation, as small stress changes may lead to a flip between S_{HMax} and S_{hmin}. At depth <6.5 km, a more homogeneous S_{HMax} orientation trending 165° is observed, while below this depth, a more heterogeneous distribution of S_{HMax} orientations is observed, with some local clusters displaying rotations up to 30° (Figure 4b). For the depth interval 6.5 km to about 8.5 km we find A_{PHI} being higher (>0.5). From 8.5 km down to about 11 km, even higher A_{PHI} values of about 0.8–0.9 are found for the entire analyzed time period, being highest during T1 (Figure 5, Table S1 in Supporting Information S1). This represents transtensional faulting regime (i.e., mixed normal and strike-slip, where $S_V \sim S_{HMax}$, Figure 5).

The stress pattern with depth described above is not spatially homogeneous. To illustrate this, we calculated A_{PHI} profiles with depth for two different regions of about 10 × 10 km^2 located south of Norcia (*E*) and Amatrice (*F*) epicenters (see Figure 5c). The transition of stress regimes with depth described above is evident for area *E* (south of Norcia) in contrast to area *F* (south of Amatrice, Figure 5c). The shallower seismicity displaying transtensional stress regime is more present in area *E*, and is more prominent during time period T1. Area *E* shows the smallest A_{PHI} values around 6 km depth, representing almost radial normal faulting stress regime, and a progressive steady increase of A_{PHI} with depth toward a transtensional stress regime (Figure 5c). Differently, the pattern is not so clear around area F, which does not display prominent seismicity <4 km, and where below 7 km a wide range of A_{PHI} values are present. The seismicity below 6.5 km tends to form a sub-horizontal band (see also Figure S3 in Supporting Information S1) and that has been previously interpreted to represent a horizontal detachment (e.g., Michele et al., 2020; Waldhauser et al., 2021). These results suggest that with depth (i.e., from 6.5 km downwards), the magnitudes of S_v and S_{HMax} tend to converge.

At wavelengths of a few km, some of the profiles perpendicular to the regional normal faults display strong lateral changes both in the S_{HMax} orientation (Figure 4b) and the A_{PHI} parameter (Figure 5b). These lateral stress variations are most prominent below 6 km, possibly coinciding with the main fault structures (Figures 4b and 5b). On the eastern side of the profiles, roughly corresponding to the footwall of the Mount Vettore Normal Fault (MVNF), larger A_{PHI} values are observed, while lower A_{PHI} values are generally visible on the hanging wall side (Figure 5c). In contrast, the variations in S_{HMax} orientation at either side of the normal fault are not consistent among the three different profiles (Figure 4c).

4.4. Temporal Evolution of Stress Parameters and Changes Before and After Large Earthquakes

In this section, we analyze the temporal evolution of the obtained stress field orientations for the different local clusters. To do so, we attributed to each seismic event the corresponding median of the S_{HMax} and A_{PHI} parameters obtained from spatial clustering. Then, we employed a moving time window of 2 days, and we estimated the median S_{HMax} and A_{PHI} parameters for all the events contained in the given time window. Given the lateral stress variations described in the previous sections, we explicitly separated the seismicity at either side of the surface projection of the MST as the main geological feature bisecting the region, as well as from different depth intervals (see Table S1 in Supporting Information S1). As the median uncertainty of S_{HMax} is 15°, the observed stress rotations mostly are at the limit of the uncertainties or just slightly larger, as observed in previous studies (e.g., Hardebeck & Okada, 2018; Martínez-Garzón et al., 2013).

Changes in S_{HMax} orientation of about 10–15° and A_{PHI} values of up to 0.2 are observed on both sides of the MST directly after the Visso and Norcia mainshocks (Figure 6). In particular, at the NW side of the MST, S_{HMax} rotates ~10° anticlockwise after the Visso and Norcia events, quickly returning to its previous value around 150° (Figure 6a). Differently, SE of the MST, the S_{HMax} orientation also rotates counterclockwise about 15° after the Norcia mainshock, coming back to its previous value after at least one month (Figure 6b). At the SE side, the A_{PHI}

Figure 4. Variation of S_{HMax} orientation with depth and time, as seen from different seismicity profiles parallel and perpendicular to the strike of the regional normal fault structures. (a) Profiles along strike (A-A′) covering a width of 2 km at each side from the plotted line in map view. Blue dashed line represents the approximate trace of the MST in cross section (Barchi et al., 2021). (b) Sections perpendicular to the normal faults, covering a thickness of 1 km at each side of the profile line in the map view. The profiles cut the seismicity around the Amatrice (B-B′) and Norcia (D-D′) epicenters. In panels (a) and (b), the plots T1–T4 correspond to the seismicity from the four analyzed time periods. (c) Map view displaying the orientation of the different profiles shown in (a) and (b) and the trace of the MST.

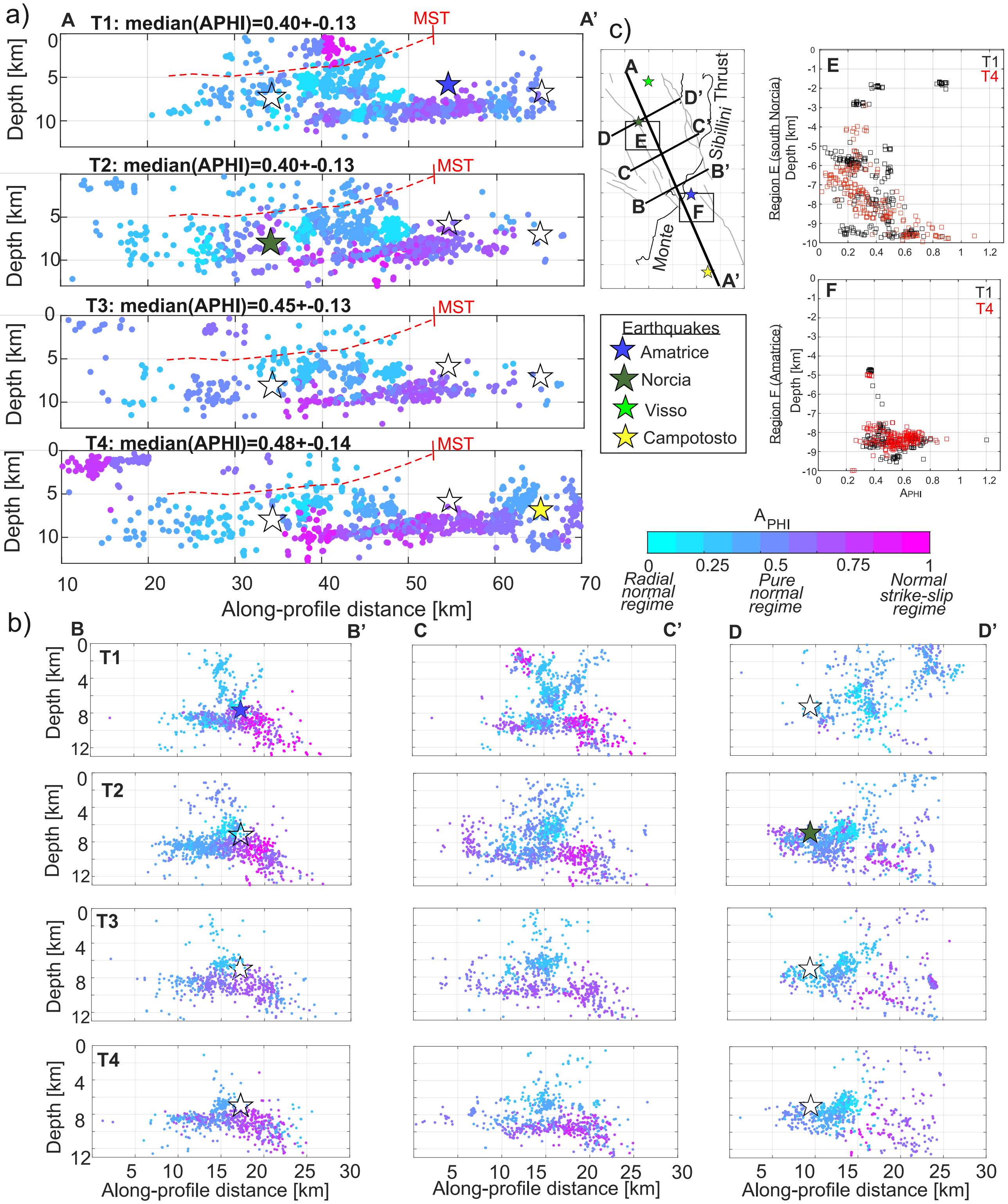

Figure 5. (a, b) Same as Figure 4 but color encoded with A_{PHI}. (c). Left: Inset map showing the profiles and the regions E and F. Right: Variation of A_{PHI} parameter with depth for regions E and F and two different temporal periods (T1 in black and T4 in red). Red dashed line represents the approximate trace of the MST in cross section (Barchi et al., 2021).

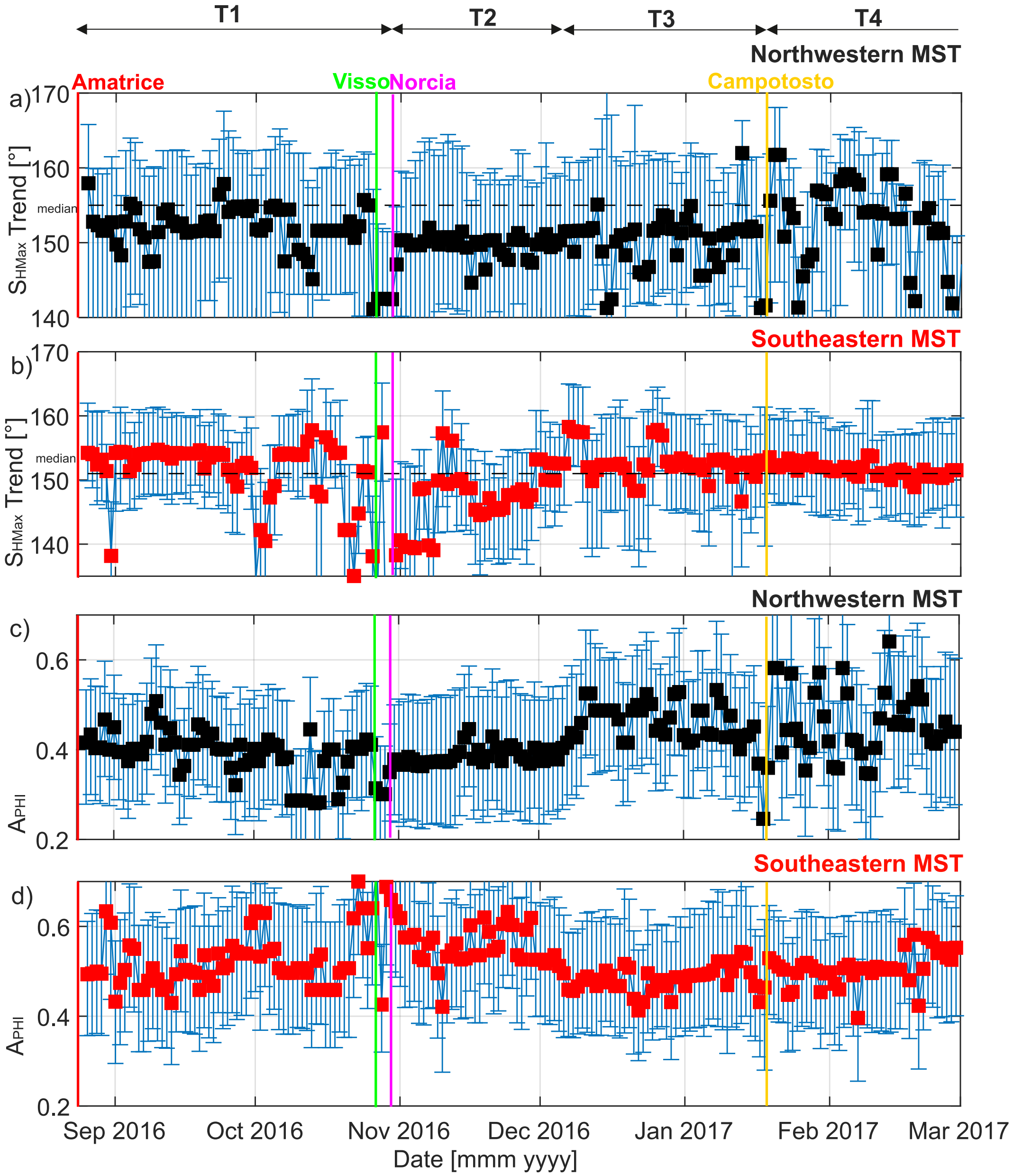

Figure 6. (a, b) S_{HMax} orientation from the seismicity activated toward the NW (back, upper panel) and SE (red, lower panel) of the MST surface trace. Vertical bars represent 95% confidence intervals derived from bootstrap resampling (see Section 3 for details). (c, d) Temporal evolution of the A_{PHI} parameter to the NW (black) and SE (red) sides of the MST surface trace, respectively. Red, green, purple, and yellow vertical lines indicate the origin time of the Amatrice, Visso, Norcia, and Campotosto mainshocks, respectively.

value around the time of these earthquakes increases by 0.2 up to 0.7, hence being slightly larger than the median uncertainties.

While both sides NW and SE show predominantly normal faulting stress regimes, the A_{PHI} parameter is larger SE of the of the surface projection of MST compared to NW (but still within the uncertainties), potentially indicating a more transtensional stress environment in the SE (Figures 6c and 6d). The difference between $\mathrm{A}_{\mathrm{PHI}}$ values from NW and SE sides is clearer during the time periods T1 and T2 between the M_{W} 6.1 Amatrice earthquake and the end of 2016 (Figures 6c and 6d).

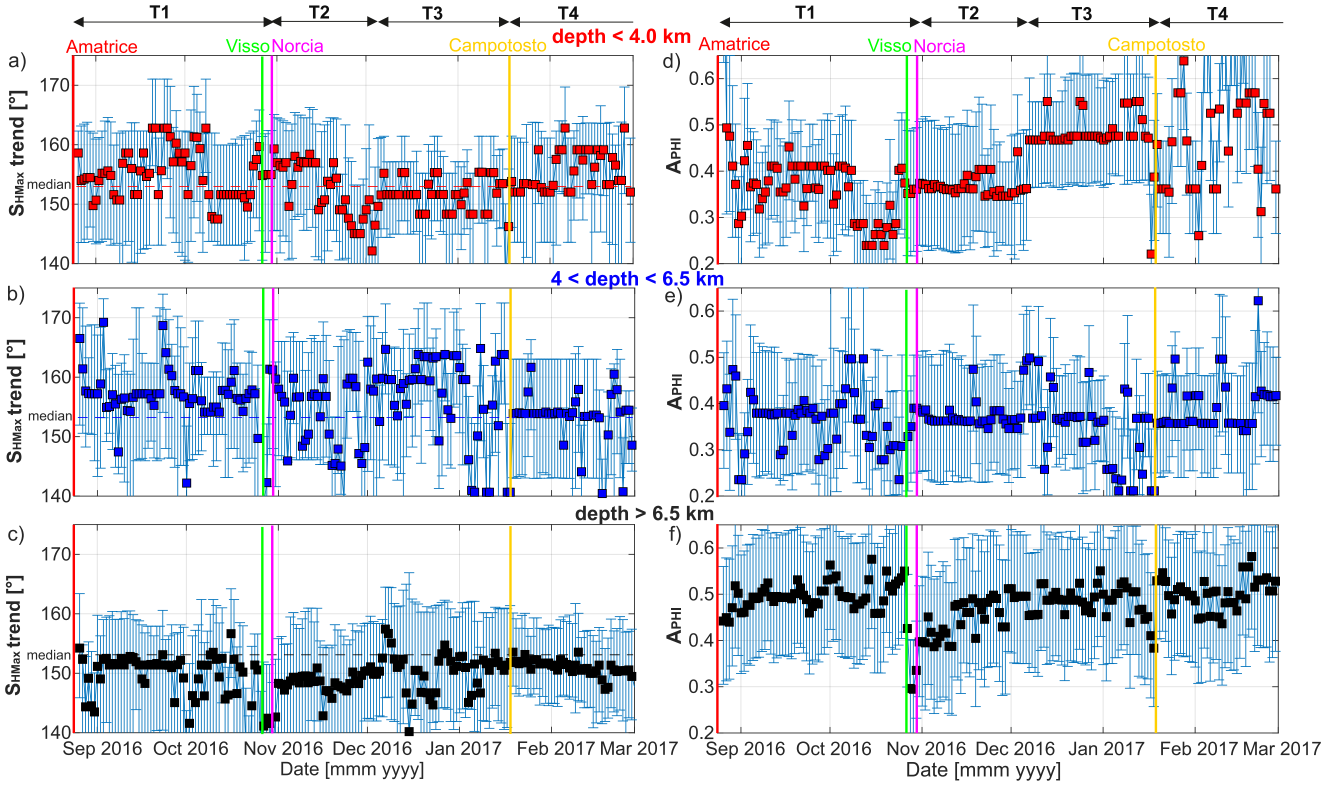

Figure 7. Temporal evolution of stress parameters from different depth ranges. (a–c) Evolution of S_{HMax} orientation from the seismicity above 4 km depth (a), between 4 and 6.5 km depth (b) and below 6.5 km depth (c). Vertical bars represent 95% confidence intervals derived from bootstrap resampling (see Section 3 for details). (d–f) Temporal evolution of the A_{PHI} parameter for the seismicity from the three depth ranges mentioned in (a–c) (red, blue, and black symbols, respectively, where $A_{\mathrm{PHI}} = 0$, $A_{\mathrm{PHI}} = 0.5$, and $A_{\mathrm{PHI}} = 1$ represent radial normal faulting, pure normal faulting and normal/strike-slip faulting stress states, respectively). Red, green, purple, and yellow vertical lines indicate the origin time of the Amatrice, Visso, Norcia, and Campotosto mainshocks, respectively. In all panels, light vertical bars represent the median 95% confidence intervals for the stress parameters in the corresponding time interval.

We also analyze the temporal evolution of S_{HMax} orientation separately for three depth ranges (Figure 7). The depth ranges are differently affected by the occurrence of Visso and Norcia mainshocks. The shallower portion (<4 km) displays a small rotation of about 12° in the S_{HMax} orientation about 1 month before the Norcia earthquake (Figure 7a). While worth to mention, such small change is not significant with respect to the median uncertainties (15°). At the same depth interval, this time period also displays a reduction of A_{PHI} from about 0.4 down to 0.25, slightly larger than the median uncertainties. Between 4 and 6.5 km depth, no significant variations of S_{HMax} and A_{PHI} are observed at the times of Visso and Norcia earthquakes. Finally, at depth >6.5 km, the most notable change is a significant decrease in the A_{PHI} from 0.55 before Visso earthquake down to 0.3. A progressive recovery toward $A_{\mathrm{PHI}} = 0.5$ is observed during the 2 weeks following the Norcia earthquake.

4.5. Stress Variability With Distance From the Amatrice and Norcia Mainshocks

The occurrence of large earthquake mainshocks results in a coseismic stress release that can significantly alter the overall local stress distribution temporarily or even permanently (e.g., Hardebeck & Okada, 2018). To further evaluate the extent of local variations in the vicinity of the largest earthquake mainshocks, we calculated a reference orientation of the principal stress axes as the median of the orientations of the principal stress axes from inversions with the trend (T_{R}) and plunge (P_{L}) angles of the principal eigenvectors being (T_{R1} 196°, P_{L1} 78°, T_{R2} 151°, P_{L2} 8° T_{R3} 62° P_{L3} 8°). Then, we estimated the difference φ_{σ} between each stress tensor and the reference tensor above. For the T1 period (from the Amatrice to the Norcia earthquakes), the largest φ_{σ} correspond to clusters of events arranged in two lines that converge near the Amatrice mainshock hypocenter (Figure 8a). This region with the largest deviation from the reference stress field orientation is located at depth >8 km (Figure 8b) and it also persisted during the entire analyzed time (Figure 8, Figures S5 and S6 in Supporting Information S1).

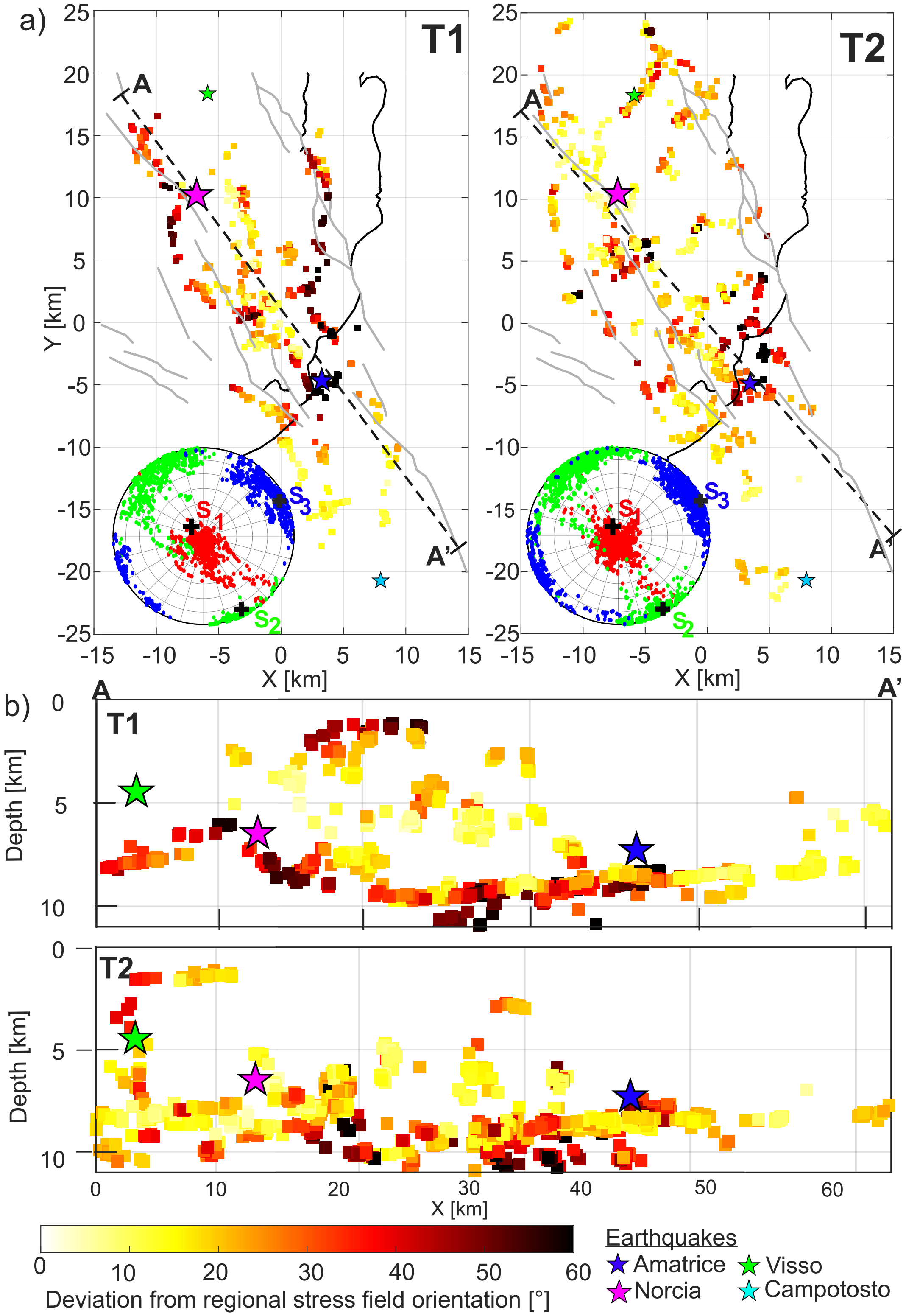

Figure 8. (a) Spatial distribution (map view) of φ_σ (defined in Section 3.1) for the time periods T1 and T2. The colored dots in the stereonets on the lower left inset of (a) show the principal stress orientations from all stress inversions in the considered time period, while the black crosses represent the regional stress. (b) Same as (a) but for the depth profile along the direction of the A-A′ profile.

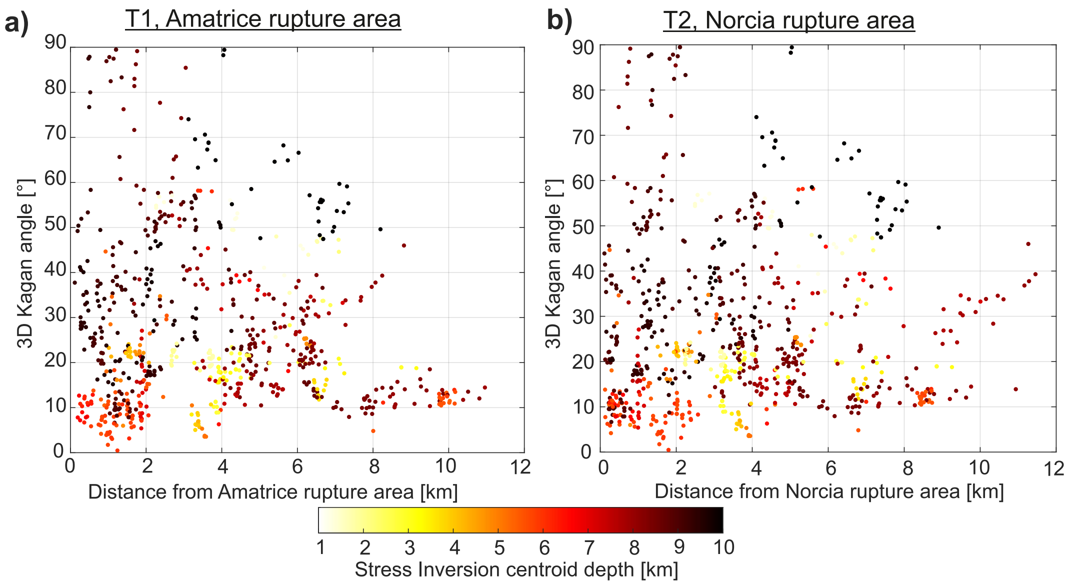

Figure 9. φ_σ as a function of distance from the rupture area of the two largest mainshocks. (a) φ_σ for the T1 period covering from the Amatrice to the Norcia earthquakes, as a function of distance from the Amatrice rupture areas. (b) φ_σ from the T2 period, as a function of distance from the Norcia rupture areas (see Figure 2 for graphical definition of time periods).

Before the Norcia mainshock (T1), a second area with large φ_σ is observed near the Norcia hypocenter and directly below at greater depth (Figure 8), which did not continue during the other time periods.

Finally, for the time periods T1 and T2, starting after the Amatrice and Norcia mainshocks, respectively, we calculate the difference between each stress tensor and the reference as a function of distance to the Amatrice and Norcia rupture areas (Scognamiglio et al., 2018; Tinti et al., 2016). After the Amatrice earthquake (T1), the largest φ_σ are located near the Amatrice rupture area, and up to 7 km away (Figure 9). $\varphi_\sigma > 40°$ are observed exclusively at depth >8 km (Figure 9a). Areas displaying small φ_σ are observed both near the Amatrice rupture as well as further away, and predominantly correspond to the shallower part of the crust (<7 km). A similar distribution can be observed with distance from the Norcia hypocenter during the period T2 (Figure 9b). Notably, similar variability with distance can be observed before the Norcia earthquake (T1). This likely suggests that these stress variations are primarily driven by structural stress heterogeneities.

5. Discussion

The 2016–2017 central Italy seismic sequence is an example of a complex series of events including three $M_W \geq 5.9$ mainshocks, namely the 2016 24 August M_W 6.0 Amatrice, 26 October M_W 5.9 Visso and 30 October M_W 6.5 Norcia, and four other $M_W \geq 5$ events that occurred in January 2017 near Campotosto. A homogeneous normal faulting stress regime with S_{HMax} predominantly oriented NW-SE has been previously reported for this area employing the largest aftershocks from the 2016–2017 central Italy sequence (Chiaraluce et al., 2017; Mariucci & Montone, 2016) as well as for the Gorzano fault in the South focusing on the events related to the January 2017 Campotosto earthquake sequence (Locchi et al., 2024). Here, we employ a deep learning catalog of earthquake focal mechanisms to illuminate spatial and temporal variations in stress parameters (e.g., S_{HMax} orientation and A_{PHI}) over local crustal volumes. We show subtle stress variations in small crustal volumes containing earthquakes separated by a median nearest-neighbor hypocentral distance of 2 km. In the following, we first constrain the magnitude of the vertical and horizontal stresses at depth based on our stress inversion results. Then, we utilize our results to elaborate on the scientific questions posed in the introduction.

5.1. Constraining Stress Magnitudes With Depth

One of the features that emerged from our analysis is a variation of the relative stress magnitudes with depth at selected portions of the study area (e.g., Region *E* near the Norcia epicenter). Comparable changes of stress regime from normal faulting toward mixed normal faulting/strike slip at depth have been reported for other

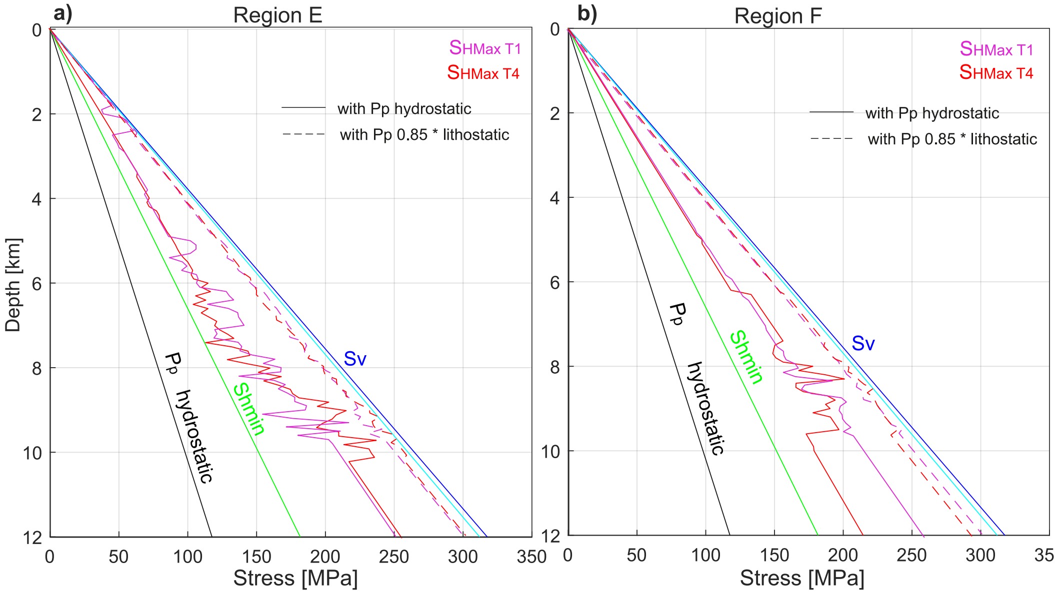

Figure 10. Distribution of median stress magnitudes with depth for the regions E (a) and F (b). Dark blue line is the estimated S_V (see text for exact parameters), while the cyan color shows the estimation by Mariucci and Montone (2016). Green and black lines denote the minimum plausible S_{hmin} assuming fault frictional equilibrium, a friction coefficient $\mu = 0.6$ and a hydrostatic pore pressure P_p, respectively. Purple and red solid lines express the S_{HMax} distribution with depth for T1 and T4 time periods, respectively, assuming hydrostatic pore pressure (see Figure 2 for graphical definition of time periods). Particularly at depth, P_p is expected to be higher than hydrostatic (see text for details). Hence, S_{HMax} results assuming $P_p = 0.85 * S_V$ are shown with dashed lines.

regions, including the Soultz-sous-Forêts area in the Rhine Graben (Cuenot et al., 2006) and the North German Basin (Heidbach et al., 2007). In these areas, regional as well as vertical variations in the principal stress magnitudes were observed, with S_{HMax} displaying a larger stress gradient with depth than S_V.

Employing various assumptions, we can place some constraints on the horizontal and vertical stress magnitudes at selected portions of the analyzed area. From the focal mechanisms of the largest events of the Central Italy sequence, borehole breakouts and seismic velocity lithospheric profiles, Mariucci and Montone (2016) analyzed the portion of the sequence between the Amatrice and Visso earthquakes. The lithostatic stress gradient in the upper 5 km was found to decrease laterally from the central Apennines (26 MPa/km) to the Adriatic foredeep (23 MPa/km), reflecting differences in stratigraphy. At 5 km depth, the vertical stress magnitudes were estimated to be about 16 MPa larger in the Apennine chain than in the Adriatic foredeep. We estimated the vertical stress magnitude with depth as the weight of the overburden at a given depth z following $S_V = \rho \cdot g \cdot z$, where ρ represents the rock density (assumed to be $\rho = 2{,}700$ kg/m^3 in the study area) and g is the gravity constant. Our vertical stress estimations (26.46 MPa/km) yield a slightly larger vertical stress gradient than the one measured from sonic logs in wells near Amatrice (Mariucci & Montone, 2016, Figure 10). We then constrain the minimum plausible S_{hmin} to allow for frictional equilibrium, assuming a friction coefficient $\mu = 0.6$ and a hydrostatic pore pressure gradient, for example, 0.4 times the vertical stress. For a normal faulting stress regime, $\frac{S_V - P_p}{S_{hmin} - P_p} \geq \left(\sqrt{1 + \mu^2} + \mu\right)^2$ (M. D. Zoback, 2007). Finally, we utilize the distribution of stress ratios with depth from our inversion results to estimate S_{HMax} following $R = \frac{S_1 - S_2}{S_1 - S_3}$ where we assumed $S_1 = S_V$, $S_2 = S_{Hmax}$, and $S_3 = S_{hmin}$. With these constraints, S_{hmin}/S_v should be constant with depth (see e.g. Figure 2 from Snee & Zoback, 2022). We utilized the R distributions with depth for the regions E and F (Figure 5c) over the time periods T1 and T4 (Figure 10a). The estimated S_{HMax} magnitude distribution with depth for the region E (south of the M_W 6.5 Norcia epicenter) shows larger fluctuations below 7 km depth. Around 9 km depth and particularly during T4, the S_{HMax} magnitude is estimated to be closer to the S_V magnitude than at the other depth intervals, hence supporting the observed mixed normal faulting and strike-slip at depth (Figure 10a). Similarly, shallower fluctuations in S_{HMax} magnitude are observed in region F (south of the M_W 6.0 Amatrice epicenter), where the magnitudes of S_{HMax} and S_V appear to be the closest at around 8 km depth (Figure 10b). These results suggest that approximately between 8.0 and 11.0 km depth, the magnitudes of S_v and S_{HMax} are closer. The resulting shear stress level τ at hypocentral depth of the mainshocks are within the range of recent estimates from Picozzi et al. (2022). For example, employing $\tau = \frac{S_V - S_{hmin}}{2}$, and assuming a depth of ~6 km for the Norcia earthquake, we obtain about 35 MPa, which is within the range [0.12, 230] MPa provided in Picozzi et al. (2022).

While these stress magnitude constraints are plausible, they are estimated based on strong assumptions. One of them is the assumption of the P_p following a hydrostatic increase with depth. More realistically, the P_p in central Italy has been suggested to be strongly compartmentalized by different faults and rock units, locally displaying some patches subjected to strong overpressure (Chiarabba et al., 2018; Chiaraluce et al., 2017; Trippetta et al., 2013). For the 2016–2017 seismic sequence, high V_p/V_s anomalies were observed in the northwestern side of the MST at about 6 km depth, as well as in the shallow portion (<4 km) in the footwall of the MVNF (Chiarabba et al., 2018). This supports the notion that the evolution of the earthquake sequence was partly controlled by patches displaying high pore fluid pressure (Gunatilake & Miller, 2022), which possibly promoted the reactivation of inherited thrust faults into normal faulting kinematics. Elevated pore pressures at depth may be expected for the lithological unit of the Triassic evaporites extending down to almost 9 km depth, where near-lithostatic CO_2 pressure has been reported previously (Chiodini & Cioni, 1989; Miller et al., 2004; Trippetta et al., 2013). To better understand the role of pore pressure on the stress magnitudes, we also repeated the S_{HMax} calculation employing $P = 0.85 * S_V$, which has been observed in selected areas of the Apennines (Collettini et al., 2008). With P_p approaching lithostatic pressure toward depth, the difference between S_{HMax} and S_v is further reduced (Figure 10).

5.2. Crustal Local Stress Heterogeneities (Wavelengths ~1–10 km) Related to Fault Discontinuities

The largest robust variations in the obtained stress patterns are observed (a) with depth. This includes a depth range between 2.5 and 8.5 km displaying pure normal faulting, toward more transtensional (mixed normal faulting and strike-slip) stress regimes at the depth ranges above and below. Variations are also observed (b) with respect to regional geological structures, and (c) related to the M_W 6.0 Amatrice and M_W 6.5 Norcia earthquakes.

The presence of fault structures and different geological domains introduce variations in the stress field, as they may represent an episodically active mechanical discontinuity separating two media with different elastic properties (e.g., Ziegler et al., 2024; M. D. Zoback, 2007). Stress differences (in the scale of 10 s of km) were observed between each side of the surface expression of the MST, coinciding with the contact of different geological domains possibly juxtaposed at a shallow dipping fault below (e.g., Figures S3 and S4 in Supporting Information S1). At an even finer scale (a few km) a stress asymmetry may also be observed on either side of the MVNF, as one of the main fault structures activated by the mainshocks from the 2016–2017 Central Italy sequence (Figures 2 and 5). To better constrain a possible connection between the observed stress discontinuity and geological structures, we overlaid our stress inversion results with detailed geological profiles for cross sections around the Norcia and Amatrice epicenters (Figure 11; Barchi et al., 2021; Collettini et al., 2022). As already observed in previous studies, the bulk of the seismicity tends to occur within the Triassic Evaporite layer (Collettini et al., 2022). Direct comparison of the seismicity with the geology confirms that after the Norcia mainshock, the region around its epicenter shows seismicity clustering in the hanging wall. Nevertheless, the scattered seismicity in the footwall of the MVNF shows larger A_{PHI} values, and hence a transtensional stress regime mixing normal and strike-slip faulting (Figure 11b). The larger A_{PHI} values on the footwall of MVNF are even more evident after the Amatrice mainshock and near its epicenter, and they appear particularly prominent between two of the locally inherited low-angle thrust faults (Figures 11c and 11d). This stress difference between either side of the fault is observed over the entire analyzed time period after the occurrence of the Amatrice and Norcia mainshocks (see e.g. Figures 4b and 5b), indicating that asymmetries in the stress pattern at either side of the faults persist for more than 1 year.

The occurrence of large mainshocks on dip-slip faults can promote stress asymmetry on either side of a fault through various mechanisms, including changes in lithological units, or stress gradients along faults that promote particular earthquake rupture patterns (Ben-Zion, 2008; Calderoni et al., 2015). In the case of the 2016 central Italy sequence, the stress discontinuity is not due to a change in the lithological unit because the Triassic evaporites extend at both sides of the MVNF (Figure 11), and it is not only driven by the co-seismic stress transfer, as it is observed to persist over the entire analyzed year. One potential mechanism is related to elastic rebound (Reid, 1911). Modeling of earthquakes in normal faulting environments shows that the dynamic rupture on a

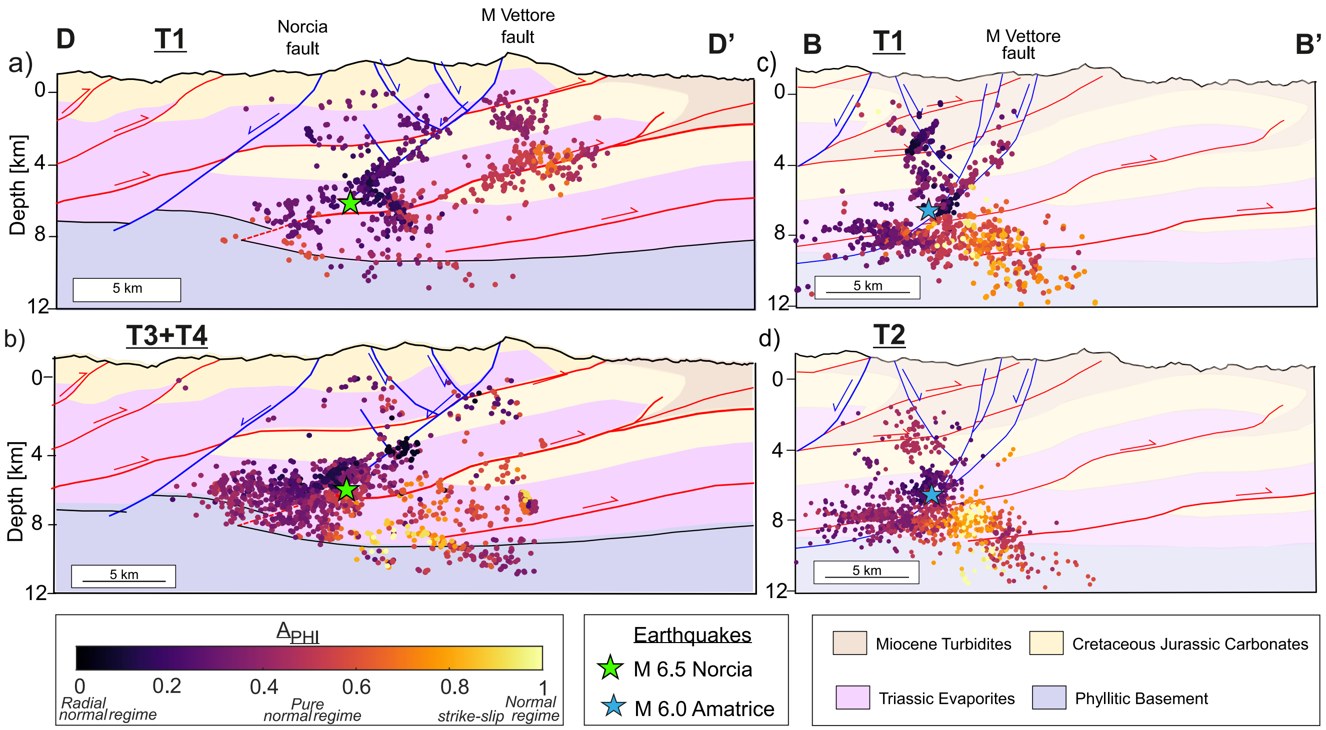

Figure 11. Seismicity color encoded with the A_{PHI} value from two profiles (5 km width) perpendicular to the normal faults crossing the Norcia (a, b) and Amatrice (c, d) epicenters, respectively, overlaid with high-resolution geological profiles for the corresponding region (Barchi et al., 2021; Collettini et al., 2022). The corresponding profiles D-D′ and B-B′ are shown in Figure 5c. The time periods represented in (a) and (b) correspond to T1 (before the Norcia mainshock) and T3 + T4 (from 5 December 2016 until the end of the data set in August 2017, respectively). The time periods represented in (c) and (d) correspond to T1 (between Amatrice and Norcia mainshock) and T2 (after Norcia mainshock), respectively.

normal fault causes substantial vertical displacement, mostly related to subsidence on the hanging wall, but also a small uplift of the footwall and remote parts of the hanging wall (Muldashev et al., 2022). For this sequence, subsidence has been quantified to be significantly larger than uplift, but small uplift in the footwall is still observed (Bignami et al., 2019). In a stress state where the magnitudes of S_{V} and S_{HMax} are similar (which in central Italy occurs particularly at depth, Figure 10) the dynamic stress changes in the footwall may lead to a slight transient decrease of the S_{V}, locally leading to a flip in the S_{V} and S_{HMax} and hence promoting oblique/strike-slip kinematics over normal faulting. The occurrence of prolonged postseismic deformation following the dynamic ruptures may contribute to sustain this stress asymmetry for long time periods, as observed here. After the M_{W} 6.0 Amatrice earthquake, postseismic deformation initiated in the region concurrent with the development of the seismic sequence (Mandler et al., 2021). The pattern of aseismic deformation extended over various fault segments and could have reached the detachment horizon at 9–11 km depth (Mandler et al., 2021). Another possible mechanism that could lead to stress asymmetries is the presence of overpressured fault compartments. However, no high pore fluid pressure patches have been resolved at 7 km depth on the footwall of the activated faults (Chiarabba et al., 2018).

As the slip along faults evolves, stress asymmetries on faults may lead to a preferential orientation for earthquake rupture propagation (Ben-Zion & Shi, 2005). In the 2016–2017 central Italy seismic sequence, the strongest earthquakes (M_{W} 6.0 Amatrice and M_{W} 6.5 Norcia) have been observed to display a preferential orientation of rupture propagation along-strike toward the NW (Calderoni et al., 2017; Scognamiglio et al., 2018; Tinti et al., 2016). In turn, these preferential rupture orientations may result in an asymmetry in the fracture and damage development and in the distribution and productivity of aftershock sequences (Ben-Zion, 2008). For example, outcrops from normal fault zones in Utah have been observed to display an asymmetry in their damage and fracture distribution, with wider damage observed on the hanging wall side than on the footwall (Berg & Skar, 2005).

5.3. Is the Stress Field Affected by Detachment Horizons at Depth?

Lithological units containing evaporites have been associated with detachment horizons due to their low shear strength, where the material is not able to effectively transmit the shear stresses from the rock units above and below (e.g., Heidbach et al., 2007; Tingay et al., 2006). In central Italy, the formation of seismically active sub-horizontal bands within the Triassic evaporites has been hypothesized to represent a basal shear zone, that is, a sub-horizontal detachment (Chiaraluce et al., 2017; Vuan et al., 2017) which also hosted significant post-seismic deformation during the 2016–2017 central Italy sequence and the following years (Mandler et al., 2021). Extension along a basal shear zone accommodated by activation of subsidiary faults with bookshelf kinematics has been suggested at the root of the MVNF and Mount Bove faults (Waldhauser et al., 2021). Differently, the correspondence of these seismicity bands with the lithology corresponding to the Triassic evaporites, has been also interpreted as distributed seismicity controlled by the mixed brittle-ductile rheology of the evaporites (Collettini et al., 2022). All of these scenarios suggest a partial mechanical decoupling between the lithology of the evaporites with the sedimentary layers above and the phyllitic basement below.

The concurrent activation of seismic activity suggests a mechanical interaction and coupling between the shallower seismicity (depth <6 km) that is mainly localized on high-angle normal faults and seismic layers at depth possibly related to an inferred deep detachment horizon (depth >6.5 km). Cause and effects of this potential coupling are still debated (Picozzi et al., 2022). At the depth range from 4 to 8 km, the geological lithology corresponds to the Triassic evaporites (Figure 11, Barchi et al., 2021; Collettini et al., 2022). The geological and mineralogical composition of the evaporites allows a broad spectrum of slip behaviors depending on the state of stress and boundary conditions, being able to host brittle failure (Scuderi et al., 2013) and ductile deformation (De Paola et al., 2009). Our results from the stress analysis with depth suggests that the lithology of the evaporites may modify the effective transmission of shear stresses through the different rock units. In particular, we documented differences between the stress state at depth >6.0 km near the detachment horizon and the stress state at shallower depth localized on high angle normal faults (Figures 4b and 5b).

However, other lines of evidence suggest an interaction of deformation between the different depth ranges and lithological units. Specifically, the first large mainshock of the sequence, the M_W 6.0 Amatrice, nucleated at the junction between the shallower high-angle faults and the detachment horizon (Figures 4, 5 and 11). In this region, both structures directly join at a depth of about 7.5 km and, according to the seismicity distribution, the shallower high-angle normal faults cut into the detachment directly (as discussed in Waldhauser et al., 2021). A similar situation is observed near the M_W 6.5 Norcia hypocenter (Figure 11). Hence, we hypothesize that the junction between the shallow normal faults and the inferred deep-seated detachment horizon, potentially releasing slip through a broad spectrum of durations and frequencies, could promote stress concentration. These stress concentrations would then represent favorable regions to nucleate large earthquakes.

5.4. Crustal Local Stress Heterogeneities (Wavelengths ~1–10 km) Related to Earthquake Rupture History

In addition to stress variations related to geological structures, lithology and depth, static and dynamic stress transfer from mainshock ruptures leads to local stress changes that can perturb the background stress field over a range of time periods (Hardebeck, 2006; Hardebeck & Okada, 2018; Yoshida et al., 2012). To remove stress perturbations caused by short term static stress transfer, the background regional stress field should be resolved with a declustered catalog (Martínez-Garzón et al., 2016). Accordingly, our results represent a superposition of the background stress field and the temporal stress changes related to the static and dynamic stress changes and other transient processes related to the evolution of a seismic sequence, including afterslip and other types of postseismic deformation or fluid propagation along main structures. In addition, the lack of sufficient nodal plane variability may result in less reliable stress inversion results (e.g., Lundstern et al., 2024).

The stress history from previous large mainshocks might be present over longer time periods (even decades, see Harris et al., 1995; Toda et al., 2005), even beyond the aftershock sequence, hence potentially affecting the background stress field of a region. In this regard, our results showed that coseismic stress transfer also affected the observed spatio-temporal stress heterogeneities. Furthermore, the stress evolution over the initial part of the sequence likely played a crucial role in controlling the subsequent spatio-temporal stress distributions and fault interaction. Previous studies suggested that the M_W 6.0 Amatrice and M_W 5.9 Visso earthquakes advanced the earthquake clock on the fault patches that ruptured with the M_W 6.5 Norcia earthquake, although they possibly also limited their size (Pino et al., 2019). After the M_W 6.0 Amatrice and M_W 6.5 Norcia earthquakes, the largest deviations from the regional stress orientations were observed at less than 7 km distance from their rupture areas (Figure 9). However, the observed stress heterogeneities with distance from the mainshocks remained over the entire analyzed time period of about 1 year (Figure 9), but we cannot exclude that they may also present before the mainshock.

Our resolved stress parameters were sensitive to the occurrence of the M_W 6.0 Amatrice, M_W 5.9 Visso, M_W 6.5 Norcia and the M_W 5–5.4 earthquake series around Campotosto (e.g., Figures 6b and 7d–f). As seismic sequences in the Apennines typically evolve over several months, with larger mainshocks not necessarily occurring at the start, tracking the temporal evolution of stress in the sequence might provide important input for time-dependent seismic hazard assessment. Some examples of these month-long extended sequences include the 1997 Colfiorito (Chiaraluce et al., 2003) and the 2009 L'Aquila events (Chiarabba et al., 2009), bounding geographically the 2016–2017 central Italy sequence to the North and South, respectively. One approach to tackle this topic is calculating the temporal evolution of *b*-value from the Gutenberg-Richter distribution, which has been proposed to be inversely proportional to differential stress (Scholz, 2015). By doing so, a *b*-value comparatively lower than during the interseismic period was reported between the M_W 6.0 Amatrice and M_W 6.5 Norcia events, which was suggested to indicate the high stress still available in the area after the Amatrice earthquake, and hence the high possibility of large upcoming events (Gulia & Wiemer, 2019, but see also Herrmann et al., 2022). As an additional proxy for crustal stress variations, Picozzi et al. (2022) utilized the long-term micro-seismicity to calculate the distribution of relative seismic energy release with respect to a background reference (energy index). With this approach, the energy index was found to be particularly high after the M_W 6.0 Amatrice and M_W 5.9 Visso earthquakes and around the future Norcia epicenter. More recently, Picozzi et al. (2024) also detected anomalies in the event-specific ground motion residuals, which were proposed to reflect, to some extent, the stress evolution of the system. Another proxy to monitor stress heterogeneity is by estimating earthquake stress drops (e.g., Kemna et al., 2021). As in Kemna et al. (2021), we also observe a temporal evolution of our stress-related parameters whose trends are punctuated by the largest events of the sequence.

The fault plane variability $\widehat{\varphi_f}$ NW of the MST about 1 month before the M_W 6.5 Norcia mainshock displayed a small decrease of about 10–15° during the time between the Amatrice and Norcia earthquakes (Figures 2a and 2c). While this field observation is too small to be statistically significant, such decrease in fault plane variability has been observed preceding macroscopic failure in laboratory experiments (Kwiatek et al., 2024). A trend toward smaller variability may indicate progressive strain localization and a more homogeneous stress field, which is favorable for earthquakes to propagate over longer distances, hence resulting in larger magnitude events (e.g., Harris, 2004). Further analysis of this parameter on the field will contribute to shed light and evaluate whether indeed strain localization and stress homogenization can be observed preceding large earthquake ruptures under various conditions.

6. Conclusions

We resolved the stress field orientation and relative stress magnitudes for the 2016–2017 central Italy seismic sequence inverting a deep learning catalog of earthquake focal mechanisms. The high resolution of the data set provided by the inclusion of focal mechanisms from smaller seismic events revealed that the presence of fault structures, contrasting lithologies and the earthquake rupture history of the region all affect crustal stress heterogeneities at the scale of 1–10 km and varying in time. The main conclusions of our analysis are the following:

1. The average S_{HMax} orientation trending N154°E and the predominance of a normal faulting stress regime, are in good agreement with previous studies and the regional extension of the Apennine Mountains (e.g., Chiaraluce et al., 2017; Lavecchia et al., 1994; Mariucci & Montone, 2016; Montone et al., 2004). However, at wavelengths of a few km, our rich data set enables us to capture local stress variations that are mainly driven by the presence of fault structures and the stress evolution within the sequence.
2. We have resolved stress variations related to different fault structures. In particular, we observed a S_{HMax} rotation of up to 30° and an A_{PHI} contrast changing from normal stress toward transtension across the Monte Sibillini Thrust surface projection (10–100 km scale). We also found similar changes (at 1–5 km scale) at either side of the MVNF at 7–8 km depth, suggesting asymmetric deformation on the normal fault at depth possibly promoted by elastic rebound.

3. We observe stress variations before and after the M_W 5.9 Visso and M_W 6.5 Norcia earthquakes, likely driven by the coseismic stress release from these earthquakes. The largest deviations in the orientation of principal stress axes from the average stress orientation are observed near the rupture areas of the two largest mainshocks and up to a distance of 5 km, quantifying the extent of the main stress change after the occurrence of the mainshocks.
4. We observe differences in the S_{HMax} orientation and A_{PHI} values between the shallower normal faults and an inferred detachment horizon at depth. However, the spatio-temporal synchronization of seismic activity between different depth ranges suggests a mechanical coupling between normal faults and a potential basal detachment.
5. Stress-related parameters show a distinct evolution between the M_W 6.0 Amatrice and M_W 6.5 Norcia events, including a decrease in fault plane variability, and A_{PHI} stress parameters. This highlights the importance of including information about the temporal evolution of stress-related parameters possibly indicating upcoming large magnitude earthquakes.

Data Availability Statement

The focal mechanism catalog employed in this analysis and its associated information are available at ETH Data Services via separate data publication (CC-BY 4.0 license) (Meier, 2025). No new software has been generated for this study.

Acknowledgments

The authors benefited from fruitful discussion with Lauro Chiaraluce, Simona Pierdominici, Grzegorz Kwiatek, Matteo Piccozzi, Mark Zoback, and Jeanne Hardebeck. We would like to thank the Editor Rachel Abercrombie, the Associate Editor, three anonymous reviewers and Jens Lundstern for carefully editing and reviewing the manuscript. In particular, the suggestions from Jens Lundstern's and his attention to detail greatly improved the clarity of the manuscript. P.M.G. acknowledges funding from the Helmholtz Association in the frame of the ERC Starting Grant 101076119 (QUAKEHUNTER). Open Access funding enabled and organized by Projekt DEAL.

References

Abolfathian, N., Martínez-Garzón, P., & Ben-Zion, Y. (2020). Variations of stress parameters in the Southern California plate boundary around the South central transverse ranges. *Journal of Geophysical Research: Solid Earth*, *125*(8), e2020JB019482. https://doi.org/10.1029/2020JB019482

Allmann, B. P., & Shearer, P. M. (2007). Spatial and temporal stress drop variations in small earthquakes near Parkfield, California. *Journal of Geophysical Research*, *112*(B4), B04305. https://doi.org/10.1029/2006JB004395

Anderson, E. M. (1951). *The dynamics of faulting and dyke formation with applications to Britain*. Hafner Pub. Co.

Barchi, M. R., Carboni, F., Michele, M., Ercoli, M., Giorgetti, C., Porreca, M., et al. (2021). The influence of subsurface geology on the distribution of earthquakes during the 2016–2017 Central Italy seismic sequence. *Tectonophysics*, *807*, 228797. https://doi.org/10.1016/j.tecto.2021.228797

Becker, D., McBrearty, I. W., Beroza, G. C., & Martínez-Garzón, P. (2024). Performance of AI-based phase picking and event association methods after the large 2023 Mw 7.8 and 7.6 Türkiye Doublet. *Bulletin of the Seismological Society of America*, *114*(5), 2457–2473. https://doi.org/10.1785/0120240017

Ben-Zion, Y. (2008). Collective behavior of earthquakes and faults: Continuum-discrete transitions, progressive evolutionary changes, and different dynamic regimes. *Reviews of Geophysics*, *46*(4), RG4006. https://doi.org/10.1029/2008RG000260

Ben-Zion, Y., Eneva, M., & Liu, Y. (2003). Large earthquake cycles and intermittent criticality on heterogeneous faults due to evolving stress and seismicity. *Journal of Geophysical Research*, *108*(B6), 2307. https://doi.org/10.1029/2002JB002121

Ben-Zion, Y., & Shi, Z. (2005). Dynamic rupture on a material interface with spontaneous generation of plastic strain in the bulk. *Earth and Planetary Science Letters*, *236*(1–2), 486–496. https://doi.org/10.1016/j.epsl.2005.03.025

Berg, S. S., & Skar, T. (2005). Controls on damage zone asymmetry of a normal fault zone: Outcrop analyses of a segment of the Moab fault, SE Utah. *Journal of Structural Geology*, *27*(10), 1803–1822. https://doi.org/10.1016/j.jsg.2005.04.012

Beroza, G. C., Segou, M., & Mostafa Mousavi, S. (2021). Machine learning and earthquake forecasting—Next steps. *Nature Communications*, *12*(1), 4761. https://doi.org/10.1038/s41467-021-24952-6

Bignami, C., Valerio, E., Carminati, E., Doglioni, C., Tizzani, P., & Lanari, R. (2019). Volume unbalance on the 2016 Amatrice—Norcia (Central Italy) seismic sequence and insights on normal fault earthquake mechanism. *Scientific Reports*, *9*(1), 4250. https://doi.org/10.1038/s41598-019-40958-z

Boncio, P., Brozzetti, F., & Lavecchia, G. (2000). Architecture and seismotectonics of a regional low-angle normal fault zone in central Italy. *Tectonics*, *19*(6), 1038–1055. https://doi.org/10.1029/2000TC900023

Bott, M. H. P. (1959). The mechanics of oblique slip faulting. *Geological Magazine*, *96*(2), 109–117. https://doi.org/10.1017/s0016756800059987

Brozzetti, F., Boncio, P., Cirillo, D., Ferrarini, F., de Nardis, R., Testa, A., et al. (2019). High-resolution field Mapping and analysis of the August–October 2016 coseismic surface faulting (Central Italy earthquakes): Slip distribution, parameterization, and comparison with global earthquakes. *Tectonics*, *38*(2), 417–439. https://doi.org/10.1029/2018TC005305

Calderoni, G., Rovelli, A., Ben-Zion, Y., & Di Giovambattista, R. (2015). Along-strike rupture directivity of earthquakes of the 2009 L'Aquila, central Italy, seismic sequence. *Geophysical Journal International*, *203*(1), 399–415. https://doi.org/10.1093/gji/ggv275

Calderoni, G., Rovelli, A., & Di Giovambattista, R. (2017). Rupture directivity of the strongest 2016–2017 Central Italy earthquakes. *Journal of Geophysical Research: Solid Earth*, *122*(11), 9118–9131. https://doi.org/10.1002/2017JB014118

Carafa, M. M. C., Galvani, A., Di Naccio, D., Kastelic, V., Di Lorenzo, C., Miccolis, S., et al. (2020). Partitioning the ongoing extension of the central Apennines (Italy): Fault slip rates and bulk deformation rates from geodetic and stress data. *Journal of Geophysical Research: Solid Earth*, *125*(7), e2019JB018956. https://doi.org/10.1029/2019JB018956

Cattania, C., & Segall, P. (2021). Precursory slow slip and foreshocks on rough faults. *Journal of Geophysical Research: Solid Earth*, *126*(4), e2020JB020430. https://doi.org/10.1029/2020JB020430

Chen, X., Kwiatek, G., Bindi, D., Becker, D., Bohnhoff, M., Cotton, F., & Martínez-Garzón, P. (2024). Stress drop variations of (A)seismic fault segments in the Sea of Marmara region (northwestern Türkiye) supported by different methodological approaches. *Bulletin of the Seismological Society of America*, *115*(3), 1016–1030. https://doi.org/10.1785/0120240128

Cheng, Y., Hauksson, E., & Ben-Zion, Y. (2023). Refined earthquake focal mechanism catalog for southern California derived with deep learning algorithms. *Journal of Geophysical Research: Solid Earth*, *128*(2), e2022JB025975. https://doi.org/10.1029/2022JB025975

Chiarabba, C., Amato, A., Anselmi, M., Baccheschi, P., Bianchi, I., Cattaneo, M., et al. (2009). The 2009 L'Aquila (central Italy) MW 6.3 earthquake: Main shock and aftershocks. *Geophysical Research Letters*, *36*(18), L18308. https://doi.org/10.1029/2009GL039627

Chiarabba, C., De Gori, P., Cattaneo, M., Spallarossa, D., & Segou, M. (2018). Faults geometry and the role of fluids in the 2016–2017 Central Italy seismic sequence. *Geophysical Research Letters*, *45*(14), 6963–6971. https://doi.org/10.1029/2018GL077485

Chiaraluce, L., Di Stefano, R., Tinti, E., Scognamiglio, L., Michele, M., Casarotti, E., et al. (2017). The 2016 Central Italy seismic sequence: A first look at the mainshocks, aftershocks, and source models. *Seismological Research Letters*, *88*(3), 757–771. https://doi.org/10.1785/0220160221

Chiaraluce, L., Ellsworth, W. L., Chiarabba, C., & Cocco, M. (2003). Imaging the complexity of an active normal fault system: The 1997 Colfiorito (central Italy) case study. *Journal of Geophysical Research*, *108*(B6), 2294. https://doi.org/10.1029/2002JB002166

Chiodini, R., & Cioni, G. (1989). Gas geobarometry for hydrothermal systems and its application to various Italian geothermal areas. *Applied Geochemistry*, *4*, 564–572.

Cochran, E. S., Page, M. T., van der Elst, N. J., Ross, Z. E., & Trugman, D. T. (2023). Fault roughness at seismogenic depths and links to earthquake behavior. *The Seismic Record*, *3*(1), 37–47. https://doi.org/10.1785/0320220043

Collettini, C., Barchi, M. R., De Paola, N., Trippetta, F., & Tinti, E. (2022). Rock and fault rheology explain differences between on fault and distributed seismicity. *Nature Communications*, *13*(1), 5627. https://doi.org/10.1038/s41467-022-33373-y

Collettini, C., Cardellini, C., Chiodini, G., De Paola, N., Holdsworth, R. E., & Smith, S. A. F. (2008). Fault weakening due to CO_2 degassing in the northern Apennines: Short- and long-term processes. *Geological Society, London, Special Publications*, *299*(1), 175–194. https://doi.org/10.1144/SP299.11

Collettini, C., Chiaraluce, L., Pucci, S., Barchi, M. R., & Cocco, M. (2005). Looking at fault reactivation matching structural geology and seismological data. *Journal of Structural Geology*, *27*(5), 937–942. https://doi.org/10.1016/j.jsg.2004.10.016

Cuenot, N., Charléty, J., Dorbath, L., & Haessler, H. (2006). Faulting mechanisms and stress regime at the European HDR site of Soultz-sous-Forêts, France. *Geothermics*, *35*(5–6), 561–575. https://doi.org/10.1016/j.geothermics.2006.11.007

Dalmayrac, B., & Molnar, P. (1981). Parallel thrust and normal faulting in Peru and constraints on the state of stress. *Earth and Planetary Science Letters*, *55*(3), 473–481. https://doi.org/10.1016/0012-821X(81)90174-6

De Paola, N., Faulkner, D. R., & Collettini, C. (2009). Brittle versus ductile deformation as the main control on the transport properties of low-porosity anhydrite rocks. *Journal of Geophysical Research*, *114*(B6), B06211. https://doi.org/10.1029/2008JB005967

Fialko, Y. (2006). Interseismic strain accumulation and the earthquake potential on the southern San Andreas fault system. *Nature*, *441*(7096), 968–971. https://doi.org/10.1038/nature04797

Gulia, L., & Wiemer, S. (2019). Real-time discrimination of earthquake foreshocks and aftershocks. *Nature*, *574*(7777), 193–199. https://doi.org/10.1038/s41586-019-1606-4

Gunatilake, T., & Miller, S. A. (2022). Spatio-temporal complexity of aftershocks in the Apennines controlled by permeability dynamics and decarbonization. *Journal of Geophysical Research: Solid Earth*, *127*(6), e2022JB024154. https://doi.org/10.1029/2022JB024154

Hardebeck, J. L., & Okada, T. (2018). Temporal stress changes caused by earthquakes: A review. *Journal of Geophysical Research: Solid Earth*, *123*(2), 1350–1365. https://doi.org/10.1002/2017JB014617

Hardebeck, J. L. (2006). Homogeneity of small-scale earthquake faulting, stress, and fault strength. *Bulletin of the Seismological Society of America*, *96*(5), 1675–1688. https://doi.org/10.1785/0120050257

Hardebeck, J. L. (2012). Coseismic and postseismic stress rotations due to great subduction zone earthquakes. *Geophysical Research Letters*, *39*(21), 157. https://doi.org/10.1029/2012GL053438

Hardebeck, J. L. (2014). The impact of static stress change, dynamic stress change, and the background stress on aftershock focal mechanisms. *Journal of Geophysical Research: Solid Earth*, *119*(11), 8266. https://doi.org/10.1002/2014JB011533

Hardebeck, J. L., & Hauksson, E. (1997). Static stress drop in the 1994 Northridge, California, aftershock sequence. *Bulletin of the Seismological Society of America*, *87*(6), 1495–1501. https://doi.org/10.1785/bssa0870061495

Hardebeck, J. L., & Michael, A. J. (2006). Damped regional-scale stress inversions: Methodology and examples for southern California and the Coalinga aftershock sequence. *Journal of Geophysical Research*, *111*(B11), B11310. https://doi.org/10.1029/2005JB004144

Harris, R. A. (2004). Numerical simulations of large earthquakes: Dynamic rupture propagation on heterogeneous faults. *Pure and Applied Geophysics*, *161*(11), 2171–2181. https://doi.org/10.1007/s00024-004-2556-8

Harris, R. A., Simpson, R. W., & Reasenberg, P. A. (1995). Influence of static stress changes on earthquake locations in southern California. *Nature*, *375*(6528), 221–224. https://doi.org/10.1038/375221a0

Heidbach, O., Reinecker, J., Tingay, M., Müller, B., Sperner, B., Fuchs, K., & Wenzel, F. (2007). Plate boundary forces are not enough: Second- and third-order stress patterns highlighted in the World Stress Map database. *Tectonics*, *26*(6), TC6014. https://doi.org/10.1029/2007TC002133

Heidbach, O., Tingay, M., Barth, A., Reinecker, J., Kurfeß, D., & Müller, B. (2010). Global crustal stress pattern based on the world stress map database release 2008. *Tectonophysics*, *482*(1–4), 3–15. https://doi.org/10.1016/j.tecto.2009.07.023

Herrmann, M., Piegari, E., & Marzocchi, W. (2022). Revealing the spatio-temporal complexity of the magnitude distribution and b-value during an earthquake sequence. *Nature Communications*, *13*, 1–10. https://doi.org/10.1038/s41467-022-32755-6

Johnson, C. W., Fu, Y., & Bürgmann, R. (2017). Seasonal water storage, stress modulation, and California seismicity. *Science*, *356*(6343), 1161–1164. https://doi.org/10.1126/science.aak9547

Kagan, Y. Y. (1991). 3-D rotation of double-couple earthquake sources. *Geophysical Journal International*, *106*(3), 709–716. https://doi.org/10.1111/j.1365-246x.1991.tb06343.x

Kemna, K. B., Verdecchia, A., & Harrington, R. M. (2021). Spatio-temporal evolution of earthquake static stress drop values in the 2016-2017 central Italy seismic sequence. *Journal of Geophysical Research: Solid Earth*, *126*(11), e2021JB022566. https://doi.org/10.1029/2021JB022566

Kwiatek, G., Martínez-Garzón, P., Goebel, T., Bohnhoff, M., Ben-Zion, Y., & Dresen, G. (2024). Intermittent criticality multi-scale processes leading to large slip events on rough laboratory faults. *Journal of Geophysical Research: Solid Earth*, *129*(3), e2023JB028411. https://doi.org/10.1029/2023JB028411

Lavecchia, G., Brozzetti, F., Barchi, M., Menichetti, M., & Keller, J. V. A. (1994). Seismotectonic zoning in east-central Italy deduced from an analysis of the Neogene to present deformations and related stress fields. *GSA Bulletin*, *106*(9), 1107–1120. https://doi.org/10.1130/0016-7606(1994)106<1107:SZIECI>2.3.CO;2

Levandowski, W., Boyd, O. S., & Ramirez-Guzmán, L. (2016). Dense lower crust elevates long-term earthquake rates in the New Madrid seismic zone. *Geophysical Research Letters*. https://doi.org/10.1002/2016GL070175

Levandowski, W., Herrmann, R. B., Briggs, R., Boyd, O., & Gold, R. (2018). An updated stress map of the continental United States reveals heterogeneous intraplate stress. *Nature Geoscience*, *11*(6), 433–437. https://doi.org/10.1038/s41561-018-0120-x

Li, P., & Cai, M. (2022). Insights into seismicity from the perspective of the crustal stress field: A comment. *Natural Hazards*, *111*(2), 1153–1178. https://doi.org/10.1007/s11069-021-05124-7

Locchi, M. E., Scognamiglio, L., Tinti, E., & Collettini, C. (2024). A large fault partially reactivated during two contiguous seismic sequences in Central Italy: The role of geometrical and frictional heterogeneities. *Tectonophysics*, *877*, 230284. https://doi.org/10.1016/j.tecto.2024.230284

Lund, B., & Townend, J. (2007). Calculating horizontal stress orientations with full or partial knowledge of the tectonic stress tensor. *Geophysical Journal International*, *170*(3), 1328–1335. https://doi.org/10.1111/j.1365-246X.2007.03468.x

Lundstern, J.-E. (2024). Recent advances in characterizing the crustal stress field and future applications of stress data: Perspectives from North America. *Geological Society, London, Special Publications*, *546*(1), 9–45. https://doi.org/10.1144/SP546-2023-195

Lundstern, J.-E., Beaucé, E., & Teran, O. J. (2024). The importance of nodal plane orientation diversity for earthquake focal mechanism stress inversions. *Geological Society, London, Special Publications*, *546*(1), 93–118. https://doi.org/10.1144/SP546-2023-63

Lundstern, J.-E., & Zoback, M. D. (2020). Multiscale variations of the crustal stress field throughout North America. *Nature Communications*, *11*(1), 1951. https://doi.org/10.1038/s41467-020-15841-5

Mancini, S., Segou, M., Werner, M. J., Parsons, T., Beroza, G., & Chiaraluce, L. (2022). On the use of high-resolution and deep-learning seismic catalogs for short-term earthquake forecasts: Potential benefits and current limitations. *Journal of Geophysical Research: Solid Earth*, *127*(11), e2022JB025202. https://doi.org/10.1029/2022JB025202

Mandler, E., Pintori, F., Gualandi, A., Anderlini, L., Serpelloni, E., & Belardinelli, M. E. (2021). Post-seismic deformation related to the 2016 Central Italy seismic sequence from GPS displacement time-series. *Journal of Geophysical Research: Solid Earth*, *126*(9), e2021JB022200. https://doi.org/10.1029/2021JB022200

Mariucci, M. T., & Montone, P. (2016). Contemporary stress field in the area of the 2016 Amatrice seismic sequence (central Italy). *Annals of Geophysics*, *59*, 9. https://doi.org/10.4401/ag-7235

Martínez-Garzón, P., Ben-Zion, Y., Abolfathian, N., Kwiatek, G., & Bohnhoff, M. (2016). A refined methodology for stress inversions of earthquake focal mechanisms. *Journal of Geophysical Research: Solid Earth*, *121*(12), 8666–8687. https://doi.org/10.1002/2016jb013493

Martínez-Garzón, P., Beroza, G. C., Bocchini, G. M., & Bohnhoff, M. (2023). Sea level changes affect seismicity rates in a hydrothermal system near Istanbul. *Geophysical Research Letters*, *50*(3), e2022GL101258. https://doi.org/10.1029/2022GL101258

Martínez-Garzón, P., Bohnhoff, M., Kwiatek, G., & Dresen, G. (2013). Stress tensor changes related to fluid injection at the Geysers geothermal field, California. *Geophysical Research Letters*, *40*, 2596–2691. https://doi.org/10.1002/grl.50438

Martínez-Garzón, P., Heidbach, O., & Bohnhoff, M. (2020). Contemporary stress and strain field in the Mediterranean from stress inversion of focal mechanisms and GPS data. *Tectonophysics*, *774*, 228286. https://doi.org/10.1016/j.tecto.2019.228286

Martínez-Garzón, P., Kwiatek, G., Ickrath, M., & Bohnhoff, M. (2014). Msatsi: A MATLAB package for stress inversion combining solid classic methodology, a new simplified user-handling, and a visualization tool. *Seismological Research Letters*, *85*(4), 896–904. https://doi.org/10.1785/0220130189

Meier, M.-A. (2025). Deep learning first motion polarity focal mechanism catalogue for the 2016 Amatrice—Norcia earthquake sequence [Dataset]. https://www.research-collection.ethz.ch/handle/20.500.11850/679151

Meier, M.-A., Lanza, F., Martínez-Garzón, P., & Chiaraluce, L. (2025). Insights into extensional tectonics from a large deep learning focal mechanism catalog. *Bulletin of the Seismological Society of America*, 1–15. https://doi.org/10.1785/0120250103

Michael, A. J. (1984). Determination of stress from slip data: Faults and folds. *Journal of Geophysical Research*, *89*(B13), 11517–11526. https://doi.org/10.1029/JB089iB13p11517

Michael, A. J. (1987). Use of focal mechanisms to determine stress: A control study. *Journal of Geophysical Research*, *92*(B1), 357–368. https://doi.org/10.1029/JB092iB01p00357

Michele, M., Chiaraluce, L., Di Stefano, R., & Waldhauser, F. (2020). Fine-scale structure of the 2016–2017 Central Italy seismic sequence from data recorded at the Italian national network. *Journal of Geophysical Research: Solid Earth*, *125*(4), e2019JB018440. https://doi.org/10.1029/2019JB018440

Miller, S. A., Collettini, C., Chiaraluce, L., Cocco, M., Barchi, M., & Kaus, B. J. P. (2004). Aftershocks driven by a high-pressure CO_2 source at depth. *Nature*, *427*(6976), 724–727. https://doi.org/10.1038/nature02251

Montone, P., Mariucci, M. T., & Pierdominici, S. (2012). The Italian present-day stress map. *Geophysical Journal International*, *189*(2), 705–716. https://doi.org/10.1111/j.1365-246X.2012.05391.x

Montone, P., Mariucci, M. T., Pondrelli, S., & Amato, A. (2004). An improved stress map for Italy and surrounding regions (central Mediterranean). *Journal of Geophysical Research*, *109*(B10), 305. https://doi.org/10.1029/2003JB002703

Muldashev, I. A., Pérez-Gussinyé, M., & Sobolev, S. V. (2022). Modeling of continental Normal Fault earthquakes. *Geochemistry, Geophysics, Geosystems*, *23*(12), e2022GC010615. https://doi.org/10.1029/2022GC010615

Nikolinakou, M. A., Flemings, P. B., & Hudec, M. R. (2014). Modeling stress evolution around a rising salt diapir. *Marine and Petroleum Geology*, *51*, 230–238. https://doi.org/10.1016/j.marpetgeo.2013.11.021

Picozzi, M., Spallarossa, D., Bindi, D., Iaccarino, A. G., & Rivalta, E. (2022). Detection of spatial and temporal stress changes during the 2016 Central Italy seismic sequence by monitoring the evolution of the energy index. *Journal of Geophysical Research: Solid Earth*, *127*(11), e2022JB025100. https://doi.org/10.1029/2022JB025100

Picozzi, M., Spallarossa, D., Iaccarino, A. G., & Bindi, D. (2024). Event-specific ground motion anomalies highlight the preparatory phase of earthquakes during the 2016–2017 Italian seismicity. *Communications Earth & Environment*, *5*(1), 1–11. https://doi.org/10.1038/s43247-024-01455-y

Pierdominici, S., & Heidbach, O. (2012). Stress field of Italy—Mean stress orientation at different depths and wave-length of the stress pattern. *Tectonophysics*, *532–535*, 301–311. https://doi.org/10.1016/j.tecto.2012.02.018

Pino, N. A., Convertito, V., & Madariaga, R. (2019). Clock advance and magnitude limitation through fault interaction: The case of the 2016 central Italy earthquake sequence. *Scientific Reports*, *9*(1), 5005. https://doi.org/10.1038/s41598-019-41453-1

Pizzi, A., Di Domenica, A., Gallovič, F., Luzi, L., & Puglia, R. (2017). Fault segmentation as constraint to the occurrence of the main shocks of the 2016 Central Italy seismic sequence. *Tectonics*, *36*(11), 2370–2387. https://doi.org/10.1002/2017TC004652

Pucci, S., De Martini, P. M., Civico, R., Villani, F., Nappi, R., Ricci, T., et al. (2017). Coseismic ruptures of the 24 August 2016, Mw 6.0 Amatrice earthquake (central Italy). *Geophysical Research Letters*, *44*(5), 2138–2147. https://doi.org/10.1002/2016GL071859

Reid, H. F. (1911). The elastic-rebound theory of earthquakes. *Bull. Dept. Geol. Univ. Calif.*, *6*, 412–444.

Ross, Z. E., Meier, M.-A., & Hauksson, E. (2018). P wave arrival picking and first-motion polarity determination with deep learning. *Journal of Geophysical Research: Solid Earth*, *123*(6), 5120–5129. https://doi.org/10.1029/2017JB015251

Rousseeuw, P. J. (1987). Silhouettes: A graphical aid to the interpretation and validation of cluster analysis. *Computational and Applied Mathematics*, *20*, 53–65. https://doi.org/10.1016/0377-0427(87)90125-7

Ruhl, C. J., Abercrombie, R. E., & Shearer, P. M. (2023). Spatially consistent small-scale stress heterogeneity revealed by the 2008 Mogul, Nevada, earthquakes. *The Seismic Record*, *3*(3), 239–248. https://doi.org/10.1785/0320230026

Schoenball, M., Dorbath, L., Gaucher, E., Wellmann, J. F., & Kohl, T. (2014). Change of stress regime during geothermal reservoir stimulation. *Geophysical Research Letters*, *41*(4), 1163–1170. https://doi.org/10.1002/2013GL058514

Scholz, C. H. (2015). On the stress dependence of the earthquake b-value. *Geophysical Research Letters*, *42*(5), 1402. https://doi.org/10.1002/2014GL062863

Scognamiglio, L., Tinti, E., Casarotti, E., Pucci, S., Villani, F., Cocco, M., et al. (2018). Complex Fault geometry and rupture dynamics of the MW 6.5, 30 October 2016, Central Italy earthquake. *Journal of Geophysical Research: Solid Earth*, *123*(4), 2943–2964. https://doi.org/10.1002/2018JB015603

Scuderi, M. M., Niemeijer, A. R., Collettini, C., & Marone, C. (2013). Frictional properties and slip stability of active faults within carbonate–evaporite sequences: The role of dolomite and anhydrite. *Earth and Planetary Science Letters*, *369–370*, 220–232. https://doi.org/10.1016/j.epsl.2013.03.024

Simpson, R. W. (1997). Quantifying Anderson's fault types. *Journal of Geophysical Research*, *102*(B8), 17909–17919. https://doi.org/10.1029/97JB01274

Skoumal, R. J., Hardebeck, J. L., & Shearer, P. M. (2024). Skhash: A Python package for computing earthquake focal mechanisms. *Seismological Research Letters*, *95*(4), 2519–2526. https://doi.org/10.1785/0220230329

Snee, J.-E. L., & Zoback, M. D. (2022). State of stress in areas of active unconventional oil and gas development in North America. *AAPG Bulletin*, *106*(2), 355–385. https://doi.org/10.1306/08102120151

Stemberk, J., Moro, G. D., Stemberk, J., Blahůt, J., Coubal, M., Košťák, B., et al. (2019). Strain monitoring of active faults in the central Apennines (Italy) during the period 2002–2017. *Tectonophysics*, *750*, 22–35. https://doi.org/10.1016/j.tecto.2018.10.033

Tan, Y. J., Waldhauser, F., Ellsworth, W. L., Zhang, M., Zhu, W., Michele, M., et al. (2021). Machine-learning-based high-resolution earthquake catalog reveals how complex fault structures were activated during the 2016–2017 Central Italy sequence. *The Seismic Record*, *1*(1), 11–19. https://doi.org/10.1785/0320210001

Tingay, M., Muller, B., Reinecker, J., & Heidbach, O. (2006). State and origin of the present-day stress field in sedimentary basins: New results from the World stress map project. In *Presented at the golden rocks 2006, the 41st U.S. Symposium on rock mechanics (USRMS), OnePetro*.

Tinti, E., Scognamiglio, L., Michelini, A., & Cocco, M. (2016). Slip heterogeneity and directivity of the ML 6.0, 2016, Amatrice earthquake estimated with rapid finite-fault inversion. *Geophysical Research Letters*, *43*(20), 10745. https://doi.org/10.1002/2016GL071263

Toda, S., Stein, R. S., Richards-Dinger, K., & Bozkurt, S. B. (2005). Forecasting the evolution of seismicity in southern California: Animations built on earthquake stress transfer. *Journal of Geophysical Research*, *110*(B5), B05S16. https://doi.org/10.1029/2004JB003415

Townend, J., & Zoback, M. D. (2004). Regional tectonic stress near the San Andreas fault in central and southern California. *Geophysical Research Letters*, *31*(15), L15S11. https://doi.org/10.1029/2003GL018918

Trippetta, F., Collettini, C., Barchi, M. R., Lupattelli, A., & Mirabella, F. A. (2013). Multidisciplinary study of a natural example of a CO_2 geological reservoir in central Italy. *International Journal of Greenhouse Gas Control*, *12*, 72–83. https://doi.org/10.1016/j.ijggc.2012.11.010

Twiss, R. J., & Unruh, J. R. (1998). Analysis of fault slip inversions: Do they constrain stress or strain rate? *Journal of Geophysical Research*, *103*(B6), 12205–12222. https://doi.org/10.1029/98JB00612

Vavryčuk, V. (2014). Iterative joint inversion for stress and fault orientations from focal mechanisms. *Geophysical Journal International*, *199*(1), 69–77. https://doi.org/10.1093/gji/ggu224

Vuan, A., Sugan, M., Chiaraluce, L., & Di Stefano, R. (2017). Loading rate variations along a Midcrustal shear zone preceding the Mw6.0 earthquake of 24 August 2016 in Central Italy. *Geophysical Research Letters*, *44*(24), 12170–12180. https://doi.org/10.1002/2017GL076223

Waldhauser, F., Michele, M., Chiaraluce, L., Di Stefano, R., & Schaff, D. P. (2021). Fault planes, Fault zone structure and detachment fragmentation resolved with high-precision aftershock locations of the 2016–2017 Central Italy sequence. *Geophysical Research Letters*, *48*(16), e2021GL092918. https://doi.org/10.1029/2021GL092918

Wallace, R. E. (1951). Geometry of shearing stress and relation to faulting. *The Journal of Geology*, *59*(2), 118–130. https://doi.org/10.1086/625831

Yin, A. (1989). Origin of regional rooted low-angle normal faults: A mechanical model and its tectonic implications. *Tectonics*, *8*(3), 469–482. https://doi.org/10.1029/tc008i003p00469

Yoshida, K., Hasegawa, A., Okada, T., Iinuma, T., Ito, Y., & Asano, Y. (2012). Stress before and after the 2011 great Tohoku-oki earthquake and induced earthquakes in inland areas of eastern Japan. *Geophysical Research Letters*, *39*(3), L03302. https://doi.org/10.1029/2011GL049729

Zaliapin, I., & Ben-Zion, Y. (2021). Perspectives on clustering and declustering of earthquakes. *Seismological Research Letters*, *93*(1), 386–401. https://doi.org/10.1785/0220210127

Zhu, W., & Beroza, G. C. (2019). PhaseNet: A deep-neural-network-based seismic arrival-time picking method. *Geophysical Journal International*, *216*(1), 261–273. https://doi.org/10.1093/gji/ggy423

Zhu, W., McBrearty, I. W., Mousavi, S. M., Ellsworth, W. L., & Beroza, G. C. (2022). Earthquake phase association using a Bayesian Gaussian mixture model. *Journal of Geophysical Research: Solid Earth*, *127*(5), e2021JB023249. https://doi.org/10.1029/2021JB023249

Ziegler, M. O., Seithel, R., Niederhuber, T., Heidbach, O., Kohl, T., Müller, B., et al. (2024). Stress state at faults: The influence of rock stiffness contrast, stress orientation, and ratio. *Solid Earth*, *15*(8), 1047–1063. https://doi.org/10.5194/se-15-1047-2024

Zoback, M. D. (2007). *Reservoir geomechanics*. Cambridge University Press.

Zoback, M. L. (1992). First- and second-order patterns of stress in the lithosphere: The World stress map project. *Journal of Geophysical Research*, *97*(B8), 11703–11728. https://doi.org/10.1029/92JB00132